Available online at www.sciencedirect.com
ScienceDirect
Journal of Computational Physics 227 (2008) 7125–7159
JOURNAL OF COMPUTATIONAL PHYSICS
www.elsevier.com/locate/jcp

High order conservative finite difference scheme for variable density low Mach number turbulent flows

Olivier Desjardins *, Guillaume Blanquart, Guillaume Balarac, Heinz Pitsch

Department of Mechanical Engineering, Stanford University, CA 94305, USA

Received 18 September 2007; received in revised form 11 March 2008; accepted 13 March 2008
Available online 28 March 2008

Abstract

The high order conservative finite difference scheme of Morinishi et al. [Y. Morinishi, O.V. Vasilyev, T. Ogi, Fully conservative finite difference scheme in cylindrical coordinates for incompressible flow simulations, J. Comput. Phys. 197 (2004) 686] is extended to simulate variable density flows in complex geometries with cylindrical or cartesian non-uniform meshes. The formulation discretely conserves mass, momentum, and kinetic energy in a periodic domain. In the presence of walls, boundary conditions that ensure primary conservation have been derived, while secondary conservation is shown to remain satisfactory. In the case of cylindrical coordinates, it is desirable to increase the order of accuracy of the convective term in the radial direction, where most gradients are often found. A straightforward centerline treatment is employed, leading to good accuracy as well as satisfactory robustness. A similar strategy is introduced to increase the order of accuracy of the viscous terms. The overall numerical scheme obtained is highly suitable for the simulation of reactive turbulent flows in realistic geometries, for it combines arbitrarily high order of accuracy, discrete conservation of mass, momentum, and energy with consistent boundary conditions. This numerical methodology is used to simulate a series of canonical turbulent flows ranging from isotropic turbulence to a variable density round jet. Both direct numerical simulation (DNS) and large eddy simulation (LES) results are presented. It is observed that higher order spatial accuracy can improve significantly the quality of the results. The error to cost ratio is analyzed in details for a few cases. The results suggest that high order schemes can be more computationally efficient than low order schemes.

Keywords: High order scheme; Finite difference scheme; Low Mach number; Variable density; Energy conservation; Conservative scheme; Cylindrical coordinates; Boundary conditions; DNS; LES

1. Motivation and objectives

Although numerical methods for fluid dynamics have been the subject of intense research for a number of years (see e.g. [1]), the accurate simulation of complex reactive turbulent flows remains a major challenge for

* Corresponding author. Tel.: +1 650 723 2938; fax: +1 650 725 3525.
E-mail address: desjardi@stanford.edu (O. Desjardins).

0021-9991/$ - see front matter © 2008 Elsevier Inc. All rights reserved.
doi:10.1016/j.jcp.2008.03.027

any computer code. While the complexity of such flows demands highly accurate schemes for the physical phenomena to be captured adequately, their potentially large density gradients and high unsteadiness require robust numerical methods for large scale simulations to be possible. However, these two properties are not easily combined in a single scheme. High order accurate finite difference schemes suffer from an aliasing error in the computation of the non-linear convection term of the Navier–Stokes equations, leading to an accumulation of kinetic energy in the smallest scales [2]. To reduce the impact of the resulting wiggles on the numerical solution, several strategies exist. De-aliasing can be performed in spectral space [3,4], even though this procedure is very costly and unpractical for complex geometries or variable density flows. Lele [5] proposed the use of high order filters in physical space. However, additional work has to be performed to ensure that the filtering operation does not affect the numerical results. Yet another strategy is to introduce upwinding in the discretization in order to stabilize the solution with numerical dissipation, but this approach has been shown to be less suited for the simulation of turbulence [6,7]. In recent years, the most successful strategy for simulating turbulence has been to employ a second order finite difference schemes on a staggered grid arrangement. This scheme, initially proposed by Harlow and Welch [8], can be shown to conserve kinetic energy discretely, therefore ensuring its robustness. In order to efficiently carry out the simulation of turbulent reactive flows, Akselvoll and Moin [9], followed by Pierce and Moin [10], adapted this scheme for variable density in cylindrical coordinates with a semi-implicit Crank–Nicolson time advancement. Similar ideas have been used successfully in other studies [11–13].

Despite its successes, this second order approach suffers from large truncation error. Indeed, the errors obtained with a second order spatial discretization are not always negligible, and can be detrimental to the accuracy of the computed results. To illustrate this point, a Gaussian-shaped vortex was convected in diagonal direction inside a periodic unit box, as shown in Fig. 1. With a 32×32 mesh, the vortex is represented on more than 10 points in its diameter. Such a spatial discretization per eddy is scarcely found in direct numerical simulations (DNS), and even less in large eddy simulations (LES). After two periods, when the vortex is back at the center of the domain, the second order scheme solution shows heavy distortions of the vortex shape, and secondary structures are starting to appear. On the other hand, the sixth order solution shows almost no difference with the exact solution.

In order to reduce the truncation error associated with low order numerical methods, high order finite difference compact schemes have been often employed [5,14]. However, direct implicit time integration cannot be easily combined with these methods in the context of low Mach number flows, therefore they cannot be easily employed in cylindrical geometries, for which the CFL restrictions at the pole ($r = 0$) are highly detrimental to the stability of numerical integration. Similarly, spectral methods are extremely challenging to use in complex geometries, and their cost exceeds greatly that of finite difference methods. In more recent works, primary conservation of mass and momentum as well as secondary conservation, i.e. conservation of kinetic energy, was combined with high order finite difference schemes for incompressible flows. In his first contribution on this subject, Morinishi et al. [15] proposed a set of fourth order conservative schemes for

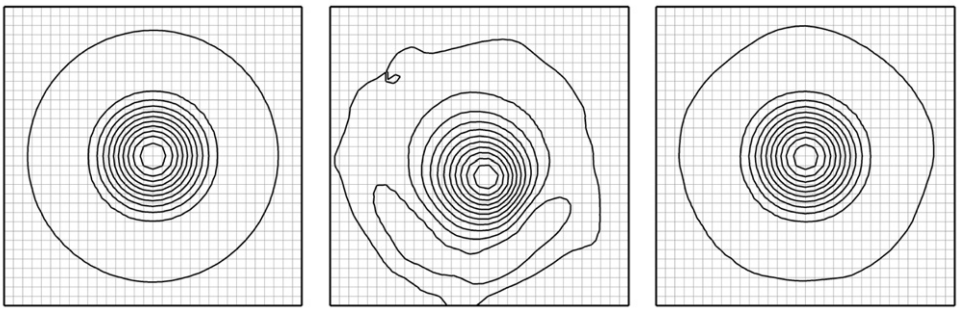

(a) Initial solution (b) Second order (c) Sixth order

Fig. 1. Contours of vorticity norm showing the effects of the order of accuracy for the diagonal convection of a Gaussian vortex for two periods on a 32×32 mesh.

uniform cartesian coordinates on both collocated and staggered grid systems. This method was used by Nicoud [16] to describe low Mach number flows using a variable coefficient Poisson equation. Vasilyev [17] extended the incompressible fourth order conservative scheme of Morinishi et al. [15] to non-uniform cartesian meshes, while retaining the conservation properties. In their latest contribution, Morinishi et al. [18] presented a fully conservative finite difference scheme of arbitrary order of accuracy for staggered grid extended to cylindrical coordinates. Such a contribution allows for new possibilities in the simulation of turbulence, where highly accurate schemes can be employed while retaining discrete primary and secondary conservation.

However, many obstacles remain in the path towards developing a numerical tool that can simulate reactive turbulent flows with such high order conservative schemes. The objective of this paper is to alleviate some of these difficulties. Towards the development of a general numerical framework for turbulent reactive DNS and LES, the following elements are addressed in the present paper:

- A fully three-dimensional, variable density version of the scheme of Morinishi et al. [18] is presented for cartesian and cylindrical geometries.
- Adequate boundary conditions are required in order to conduct more complex simulations. A consistent approach for implementing boundary conditions is presented and tested.
- A strategy for the implementation of a high order viscous term is proposed, along with boundary conditions.
- With these possibilities at our disposal, the question of the choice of the best order of accuracy can be raised. In order to provide some insights to this answer, several canonical flows have been simulated in order to establish best practice, and the results are discussed.

This paper is organized as follows: The next section presents the equations that are considered in this work. Section 3 introduces the variable density formulation of the scheme of Morinishi et al. [18], along with test cases to verify the accuracy and conservation of the method in the presence of a non-uniform mesh and density variations. Section 4 deals with the implementation of boundary conditions, as well as the consequence in terms of energy conservation. Section 5 presents a discussion on the centerline treatment that can be used to handle the $r = 0$ singularity in cylindrical coordinates for high order schemes. Section 6 introduces an arbitrarily high order accurate viscous scheme along with adequate boundary conditions. The higher order issues addressed in sections four to six can be discussed both for variable and constant density flows, but are considered here only for the variable density case. Finally, in the last section, the full numerical scheme is employed to simulate a range of canonical test problems that include turbulent and laminar cases, constant and variable density cases, as well as LES and DNS. In this work, all the simulations have been performed by an in-house code named "NGA", where the numerical methods presented here have been implemented in parallel using message passing interface (MPI).

2. Governing equations

We are interested in solving the variable density, low Mach number Navier–Stokes equations. Conservation of mass reads

$$\frac{\partial \rho}{\partial t} + \nabla \cdot \rho \mathbf{u} = 0, \tag{1}$$

where $\mathbf{u}$ is the velocity vector and ρ the fluid density. Conservation of momentum is written as

$$\frac{\partial \rho \mathbf{u}}{\partial t} + \nabla \cdot (\rho \mathbf{u} \otimes \mathbf{u}) = -\nabla p + \nabla \cdot \boldsymbol{\sigma}, \tag{2}$$

where p is the pressure, and

$$\boldsymbol{\sigma} = \mu(\nabla \mathbf{u} + {}^t\nabla \mathbf{u}) - \frac{2}{3}\mu \nabla \cdot \mathbf{u}\mathbf{I}. \tag{3}$$

Here, μ is the dynamic viscosity and I is the identity tensor. The following symbolic definitions can be introduced:

$$\begin{aligned} &(\text{cont}) = \nabla \cdot \rho \mathbf{u}, \quad (\text{div}) = \nabla \cdot (\rho \mathbf{u} \otimes \mathbf{u}), \\ &(\text{pres}) = \nabla p, \quad \text{and} \quad (\text{visc}) = \nabla \cdot \boldsymbol{\sigma}. \end{aligned} \tag{4}$$

The momentum vector will be written $\mathbf{g} = \rho \mathbf{u}$.

In this work, it will be assumed that the density is obtained through a mixing or combustion model that depends on flow variables and transported scalars. A typical model is to express the density as a function of a conserved scalar Z that represents mixing [19] and for which a transport equation is solved:

$$\frac{\partial \rho Z}{\partial t} + \nabla \cdot (\rho \mathbf{u} Z) = \nabla \cdot (\rho D_Z \nabla Z), \tag{5}$$

where D_Z is the diffusivity. In the remainder of this work, we will use $\rho = \hat{\rho}(Z)$ as a combustion model, keeping in mind that the actually applied model may depend on other variables. Similarly, the viscosity and diffusivity will be obtained through $\mu = \hat{\mu}(Z)$ and $D_Z = \widehat{D}_Z(Z)$. The additional symbolic definition can be introduced:

$$(\text{scal}) = \nabla \cdot (\rho \mathbf{u} Z). \tag{6}$$

3. Variable density conservative finite difference scheme

In this section, we will present the variable density version of the scheme proposed by Morinishi et al. [18] for cylindrical coordinates. Round and planar geometries being both of high interest, the scheme will be presented for both cylindrical and cartesian coordinate systems.

3.1. Coordinate system

The physical space is described by a coordinate system $\mathbf{x} = (x_1, x_2, x_3)$ that can be cartesian, i.e. $(x_1, x_2, x_3) = (x, y, z)$ or cylindrical, i.e. $(x_1, x_2, x_3) = (x, r, \theta)$. The physical space is mapped into the uniform computational space of unity spacing $\boldsymbol{\zeta} = (\zeta_1, \zeta_2, \zeta_3)$. Associated with this mapping, scaling factors can be defined by differentiating the physical space with respect to the computational space, leading to

$$h_1 = \frac{\mathrm{d}x_1}{\mathrm{d}\zeta_1}, \quad h_2 = \frac{\mathrm{d}x_2}{\mathrm{d}\zeta_2}, \quad h_3 = \frac{\mathrm{d}x_3}{\mathrm{d}\zeta_3} \tag{7}$$

for cartesian coordinates and

$$h_1 = \frac{\mathrm{d}x_1}{\mathrm{d}\zeta_1}, \quad h_2 = \frac{\mathrm{d}x_2}{\mathrm{d}\zeta_2}, \quad h_3 = x_2 \frac{\mathrm{d}x_3}{\mathrm{d}\zeta_3} \tag{8}$$

for cylindrical coordinates. From the scaling factors, the Jacobian can be defined by

$$J = h_1 h_2 h_3. \tag{9}$$

For the sake of generality of notation, the velocity will be written $\mathbf{u} = {}^t(u_1, u_2, u_3)$ where in cartesian coordinates $(u_1, u_2, u_3) = (u_x, u_y, u_z)$, while in cylindrical coordinates we write $(u_1, u_2, u_3) = (u_x, u_r, u_\theta)$. The same notation is introduced for the momentum vector $\mathbf{g} = {}^t(g_1, g_2, g_3)$. The variables are staggered on the computational mesh, their positions are shown in Fig. 2. Note that all scalar quantities (Z, ρ, μ, D_Z) are stored at the cell center like the pressure.

3.2. Discrete operators

For reference, the discrete operators defined in [18] are reintroduced here. The second order interpolation with stencil size n in the ζ_1 direction acting on a quantity ϕ is expressed by

$$\bar{\phi}^{n\zeta_1}(\zeta_1, \zeta_2, \zeta_3) = \frac{\phi(\zeta_1 + n/2, \zeta_2, \zeta_3) + \phi(\zeta_1 - n/2, \zeta_2, \zeta_3)}{2}. \tag{10}$$

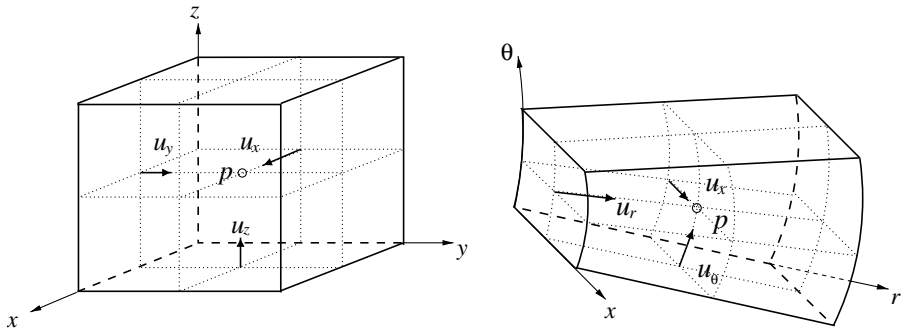

(a) Cartesian coordinates (b) Cylindrical coordinates

Fig. 2. Staggered variable positions.

$\bar{\phi}^{n\zeta_2}$ and $\bar{\phi}^{n\zeta_3}$ are defined in the same manner. The second order differentiation of stencil size n in the ζ_1 direction of the quantity ϕ is computed by

$$\frac{\delta_n \phi}{\delta_n \zeta_1}(\zeta_1,\zeta_2,\zeta_3) = \frac{\phi(\zeta_1 + n/2,\zeta_2,\zeta_3) - \phi(\zeta_1 - n/2,\zeta_2,\zeta_3)}{n}. \tag{11}$$

$\frac{\delta_n \phi}{\delta_n \zeta_2}$ and $\frac{\delta_n \phi}{\delta_n \zeta_3}$ are defined in the same manner. To construct the nth order accurate operators, interpolation weights α_l have to be computed by solving

$$\sum_{l=1}^{n/2} (2l-1)^{2(i-1)} \alpha_l = \delta_{i1} \quad \text{for } i \in [\![1, n/2]\!], \tag{12}$$

where δ_{ij} is the Kronecker delta. The nth order interpolation in the ζ_i direction for $i \in \{1,2,3\}$ is then defined by

$$\bar{\phi}^{n\text{th}\zeta_i} = \sum_{l=1}^{n/2} \alpha_l \bar{\phi}^{(2l-1)\zeta_i}. \tag{13}$$

Similarly, the nth order differentiation operator will be

$$\frac{\delta_{n\text{th}} \phi}{\delta_{n\text{th}} \zeta_i} = \sum_{l=1}^{n/2} \alpha_l \frac{\delta_{(2l-1)} \phi}{\delta_{(2l-1)} \zeta_i}. \tag{14}$$

The benefit of using these high order accurate staggered operators can be readily seen by looking at the modified wave number diagrams shown in Fig. 3. Here, the modified wave number has been computed for the staggered differentiation operator and for the combination of the staggered differentiation with the staggered interpolation operator, which corresponds to the collocated differentiation operator. These are typically the two types of operators which will be used in the solution of the Navier–Stokes equations. It can be observed from these graphs that regardless of the operator type, it is beneficial to use high order operators, for the dispersive errors are significantly reduced, especially at high wave numbers. Of course, the staggered operator has significantly less errors than the collocated operator. Also, dissipative errors are inexistent here since all operators are centered. In order to further analyze the *a priori* properties of these schemes, the study of aliasing errors proposed by Kravchenko and Moin [2] is extended here to include the fourth and sixth order schemes. By doing a Fourier analysis of the non-linear term computed by the different schemes, the contribution due to the aliasing effect can be extracted. This is performed on a given mesh and assuming a prescribed Von Karman spectrum for the velocity, following the procedure of Kravchenko and Moin [2]. The computed aliasing error as a function of the wave number is shown in Fig. 4. It is clear

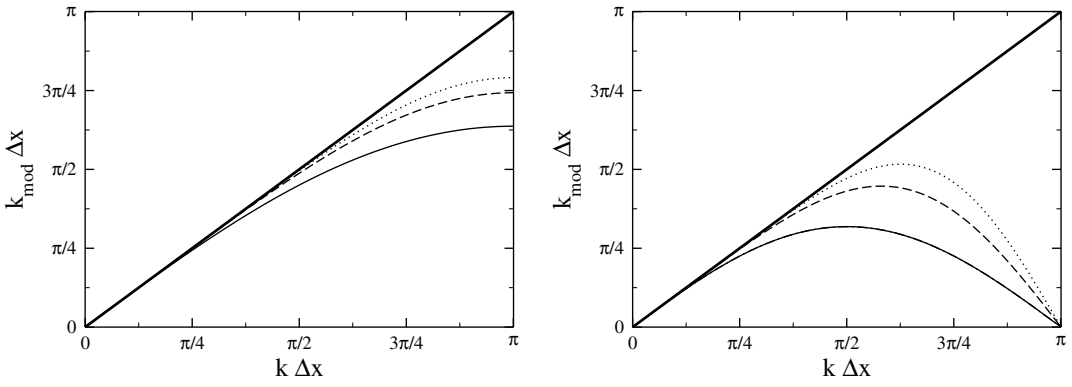

Fig. 3. Modified wave number diagram: exact (thick line); second (solid line), fourth (dashed line) and sixth (dotted line) orders.

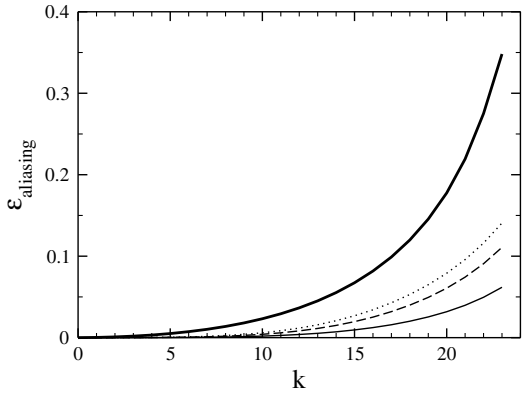

Fig. 4. Aliasing error: spectral (thick line); second (solid line), fourth (dashed line) and sixth (dotted line) orders.

that a non-dealiased spectral scheme will give the most errors in this case, which is what is indeed seen in Fig. 4. The second order scheme is less prone to these errors, followed by the fourth order and the sixth order schemes. These results suggest that the higher the order of accuracy, the more the schemes exhibit a spectral behavior.

3.3. Numerical discretization

Using these expressions, the divergence form of the convective term of the Navier–Stokes equations transformed into computational space [18] will be written at any even order of accuracy n

$$(\text{div-}n)_{x_1} = \sum_{i=1}^{3}\left(\frac{1}{\overline{J}^{1\zeta_1}}\sum_{l=1}^{n/2}\alpha_l\frac{\delta_{(2l-1)}}{\delta_{(2l-1)\zeta_i}}\left[\overline{\left(\frac{J}{h_i}g_i\right)}^{n\text{th}\zeta_1}\overline{u_1}^{(2l-1)\zeta_i}\right]\right), \tag{15}$$

$$(\text{div-}n)_{x_2} = \sum_{i=1}^{3}\left(\frac{1}{\overline{J}^{1\zeta_2}}\sum_{l=1}^{n/2}\alpha_l\frac{\delta_{(2l-1)}}{\delta_{(2l-1)\zeta_i}}\left[\overline{\left(\frac{J}{h_i}g_i\right)}^{n\text{th}\zeta_2}\overline{u_2}^{(2l-1)\zeta_i}\right]\right) - \epsilon\frac{1}{\overline{J}^{1\zeta_2}}\overline{\left(\frac{J}{x_2}\overline{g_3}^{n\text{th}\zeta_3}\overline{u_3}^{n\text{th}\zeta_3}\right)}^{n\text{th}\zeta_2}, \tag{16}$$

$$(\text{div-}n)_{x_3} = \sum_{i=1}^{3}\left(\frac{1}{\overline{J}^{1\zeta_3}}\sum_{l=1}^{n/2}\alpha_l\frac{\delta_{(2l-1)}}{\delta_{(2l-1)\zeta_i}}\left[\overline{\left(\frac{J}{h_i}g_i\right)}^{n\text{th}\zeta_3}\overline{u_3}^{(2l-1)\zeta_i}\right]\right) + \epsilon\frac{1}{\overline{J}^{1\zeta_3}}\overline{\left(\frac{J}{x_2}\overline{g_2}^{n\text{th}\zeta_2}\overline{u_3}^{n\text{th}\zeta_3}\right)}^{n\text{th}\zeta_3}, \tag{17}$$

where ϵ is zero in cartesian coordinates and one in cylindrical coordinates.[1]

The divergence of the momentum vector that appears in the continuity equation will be written

$$(\text{cont-}n) = \sum_{i=1}^{3} \left(\frac{1}{J} \frac{\delta_{n\text{th}}}{\delta_{n\text{th}}\zeta_i} \left[\frac{J}{h_i} g_i \right] \right). \tag{18}$$

Finally, the pressure gradient will be expressed as

$$(\text{pres-}n)_{x_i} = \frac{J}{\overline{J}^{1\zeta_i}} \frac{1}{h_i} \frac{\delta_{n\text{th}} p}{\delta_{n\text{th}}\zeta_i}. \tag{19}$$

The Jacobian inverse that appears in front of every term in Eqs. (15)–(17) and (19) can be evaluated by a number of methods. In our numerical tests, very little difference on the resulting order of accuracy was obtained by changing the way this term in computed. As a result, we chose to express it similarly to Morinishi et al. [18] by using second order interpolation.

3.4. Relationship between velocity and momentum

Because of the staggering of the variables in space, the velocity components and the density are not located at the same position. As a result, the ith component of the momentum vector is discretely expressed by

$$g_i = \overline{\rho}^{2\text{ndx}_i} u_i, \tag{20}$$

where the interpolation operator acting on the density is a second order interpolation in physical space that will be introduced in Section 6. A similar strategy is employed to compute the interpolated values of viscosity and diffusivity. Unbounded values of interpolated density are highly detrimental to the robustness of the variable density scheme. In order to avoid this issue, the density interpolation should be total variation diminishing (TVD). This is most easily achieved by limiting ourselves to a second order interpolation, regardless of the order of accuracy of the rest of the scheme. While a higher order TVD interpolation could be designed, our numerical experiments showed little effect of the second order density interpolation on the quality of the results.

[1] For the sake of completeness, we include here the pseudo-code that is used to calculate in the array DIVX the convective term in the ζ_1 direction defined by Eq. (15) at any order n:

```
for i = 1 to N_x do
  for j = 1 to N_y do
    for k = 1 to N_z do
      DIVX(i,j,k) ⇐ 0
      for st = −n/2 to n/2 − 1 do
        DIVX(i,j,k) ⇐ DIVX(i,j,k) + 1/2div(i,j,k,st)G1(i+st,j,k)(U1(i+2st+1,j,k) + U1(i,j,k))
      end for
      for st = −n/2 + 1 to n/2 do
        DIVX(i,j,k) ⇐ DIVX(i,j,k) + 1/2div(i,j,k,st)G2(i,j+st,k)(U1(i,j+2st−1,k) + U1(i,j,k))
        DIVX(i,j,k) ⇐ DIVX(i,j,k) + 1/2div(i,j,k,st)G3(i,j,k+st)(U1(i,j,k+2st−1) + U1(i,j,k))
      end for
    end for
  end for
end for
```

The array U1 contains the first component of the velocity vector, while G1, G2, and G3 are the three components of the momentum vector. The array div contains the operator defined by Eq. (14) divided by $\overline{J}^{1\zeta_1}$ at every (i,j,k) location. A schematic of the procedure can also be found in Fig. 9.

3.5. Discretization of the scalar transport equation

While not the primary objective of this paper, the discretization of the scalar transport equation is included here for the sake of completeness. The advection of a scalar quantity is discretely written

$$(\text{scal-}n) = \sum_{i=1}^{3} \left(\frac{1}{J} \frac{\delta_{n\text{th}}}{\delta_{n\text{th}}\zeta_i} \left[\frac{J}{h_i} g_i \overline{\overline{Z}}^{\zeta_i} \right] \right), \tag{21}$$

where $\overline{\overline{\phi}}^{\zeta_i}$ represents the interpolation of a scalar quantity ϕ to a cell face in the ζ_i direction. This interpolation is specific to the scalar quantities, and has to be considered carefully. Indeed, the accuracy of scalar transport quantities is a critical issue in turbulent reactive simulations. The boundedness of a conserved scalar is often highly desirable for the stability of combustion models, and therefore TVD schemes such as third order or fifth order WENO [20,21] can be considered as schemes of choice, despite the numerical diffusion they induce. While not TVD, high order upwind central schemes (HOUC) [22] of any odd order are also of great interest, for they allow to reach high order accuracy, while the slight upwinding helps obtain a smooth scalar field. Two classes of HOUC schemes have been implemented, namely a finite volume type interpolation ($\text{HOUC}^n_{\text{FV}}$) and a finite difference type interpolation ($\text{HOUC}^n_{\text{FD}}$). In both cases, n has to be odd to allow for upwinding. To obtain the nth order accuracy for the scalar advection, the $\text{HOUC}^n_{\text{FV}}$ has to be combined with a second order divergence operator, while the $\text{HOUC}^n_{\text{FD}}$ has to be combined with an mth order divergence operator, where $m > n$. These properties of the scalar transport schemes, as well as the required stencil size, are summarized in Table 1. Note for example that a third order HOUC corresponds to Leonard's QUICK scheme [23].

3.6. Temporal integration

The Navier–Stokes equations are solved using the second order semi-implicit Crank–Nicolson scheme of Pierce and Moin [10]. Inspired by the classical fractional step approach [24], this iterative time advancement scheme uses staggering in time between the momentum field and the scalar and density fields. The scalars are advanced first, the density field is updated, and the momentum equations are then advanced. The pressure Poisson equation is then solved to enforce continuity using a combination of spectral methods, Krylov-based methods [25], and multi-grid methods [26], depending on the geometry of the problem. In order to relax the CFL conditions that can limit very severely the time step size in cylindrical coordinates, an implicit correction is computed for the scalar and momentum equations, using an approximate factorization technique similar to the one used by Choi and Moin [27]. This implicit correction requires the solution of a poly-diagonal system in parallel for each velocity component and for each spatial direction that is treated implicitly. The number of diagonals in the linear problem depends on the order of the scheme. For example, the second order formulation leads to a tri-diagonal system, while the fourth order formulation leads to a hepta-diagonal problem. This semi-implicit approach combines the benefit of conserving kinetic energy discretely in time in the case of constant density, as discussed in Ham et al. [28], and of allowing to run with greatly relaxed CFL restrictions. It should however be noted that in the case of variable density, this methodology fails to discretely conserve kinetic energy. Indeed, Pierce and Moin [10] showed that a second order temporal error that is proportional to the time derivative of density is introduced.

Table 1
Properties of the different scalar transport schemes used

Scalar scheme	Divergence order	Global accuracy	TVD property	Total stencil length
$\text{HOUC}^n_{\text{FV}}$	2	n	×	$n+2$
$\text{HOUC}^n_{\text{FD}}$	m	$\min(n,m)$	×	$n+m$
WENO-3	2	up to 3	✓	5
WENO-5	2	up to 5	✓	7

3.7. Conservation properties

For all terms written in divergence form, it has been noted that conservation is achieved *a priori* [18]. As a result, quantities such as mass, momentum, or fuel mass fraction solved using a scalar transport equation are conserved discretely. However, to prove discrete energy conservation, a transport equation for the kinetic energy should be written. As for its analytical counterpart, this transport equation is based on the continuity and momentum equations. If all terms in the kinetic energy equation can be written in the form of a divergence, then kinetic energy is discretely conserved.

As already pointed out by Morinishi et al. [15] and Vasilyev [17], local kinetic energy is ambiguous to define in a staggered grid arrangement, as the velocity components are found at different locations. The square of the velocity components can be evaluated at the center of each of the faces and then interpolated back at the cell center. This way, the discrete kinetic energy should be defined as

$$K = \frac{1}{2J}\sum_{i=1}^{3}\overline{\overline{J}^{1\zeta_i} g_i u_i}, \tag{22}$$

where $\bar{\phi}$ represents a cell-centered value of ϕ obtained by any interpolation technique. As the mesh is non-uniform, the Jacobians have to be reintroduced to account for stretching. The discrete transport equation for the kinetic energy will be deduced from the discrete transport equations for the velocity components, by combining the approaches introduced by Morinishi et al. [15,18]. For instance, after multiplying the convective term for the first component of the velocity vector by the first velocity component, we shall obtain

$$\overline{J}^{1\zeta_1} u_1(\text{div-}n)_{x_1} = \sum_{i=1}^{3}\left(\sum_{l=1}^{n/2}\alpha_l \frac{\delta_{(2l-1)}}{\delta_{(2l-1)\zeta_i}}\left[\overline{\left(\frac{J}{h_i}g_i\right)}^{n\text{th}\zeta_1}\widetilde{u_1 u_1}^{(2l-1)\zeta_i}\right]\right) + \frac{1}{2}u_1^2\overline{(\text{cont-}n)}^{n\text{th}\zeta_1}, \tag{23}$$

where a new interpolation operator has been introduced, which is defined as

$$\widetilde{\phi\psi}^{n\zeta_1}(\zeta_1,\zeta_2,\zeta_3) = \frac{1}{2}\phi(\zeta_1+n/2,\zeta_2,\zeta_3)\psi(\zeta_1-n/2,\zeta_2,\zeta_3) + \frac{1}{2}\phi(\zeta_1-n/2,\zeta_2,\zeta_3)\psi(\zeta_1+n/2,\zeta_2,\zeta_3). \tag{24}$$

As in the case of constant density, the convective term of the momentum equation will discretely conserve kinetic energy only if the continuity equation is exactly satisfied.

On the other hand, the pressure term differs significantly from the case of constant density and further analysis is required. Morinishi et al. [15] introduced an interpolation scheme in order to rewrite the pressure term

$$\overline{\overline{J}^{1\zeta_1} u_i(\text{pres-}n)_{x_i}} = \sum_{l=1}^{n/2}\alpha_l u_i \overline{\frac{\delta_{(2l-1)}p}{\delta_{(2l-1)\zeta_i}}}^{(2l-1)\zeta_i} \tag{25}$$

$$= \sum_{l=1}^{n/2}\alpha_l \frac{\delta_{(2l-1)}}{\delta_{(2l-1)\zeta_i}}(u_i\bar{p}^{(2l-1)\zeta_i}) - p\frac{\delta_{n\text{th}}}{\delta_{n\text{th}\zeta_i}}\left[\frac{J}{h_i}u_i\right]. \tag{26}$$

With this new interpolation operator, it is straightforward to see that the pressure term conserves kinetic energy in the case of constant density. However, in the case of variable density, the last term is not zero as the continuity equation does not imply a divergence free velocity field. This pressure-dilatation term $(-p\nabla\cdot\mathbf{u})$ is of course physical, since it exists also in the continuous transport equation for kinetic energy. It represents the energy transfer between the kinetic energy and the internal energy through the work of pressure in the presence of dilatation. It should be noted however that no equation is solved for the internal energy, therefore there exists no counterpart to the pressure-dilatation term. As a result, numerical errors in kinetic energy may be able to accumulate through this term. This phenomenon, referred to as spurious heat release [10], is caused by the discrete discrepancy that exists between the continuity equation (Eq. (1)) and the scalar transport equation (Eq. (5)), as will be discussed in further details in Section 3.8.3. This issue is caused by the combined effects of the high order formulation and the variable density aspect of the flows considered.

3.8. Test cases

Numerical tests are conducted to check that adequate order of accuracy as well as conservation properties are obtained.

3.8.1. High order accuracy

In order to verify the correct behavior of the numerical scheme, the order of accuracy is evaluated by convecting a circular vortex inside a two-dimensional unit box $[-0.5, 0.5] \times [-0.5, 0.5]$ with periodic boundary conditions. The initial velocity field is given by

$$\mathbf{u}(x,y) = \begin{pmatrix} 1 - \frac{y}{2} e^{-(x^2+y^2)/a^2} \\ \frac{x}{2} e^{-(x^2+y^2)/a^2} \end{pmatrix}, \tag{27}$$

where the value of a is set to 0.2. The mesh is uniform in the y direction, but has stretching in the x direction. The mesh is given as $x = x_0 + s_x \sin(2\pi x_0)$, where x_0 is uniform in $[-0.5, 0.5]$. The value of s_x is set to 0.15, leading to very strong stretching. The simulation is performed at a constant CFL number of 0.01 for one time unit, when the vortex should be back at its original location, and the L_∞ norm of the error between the computed axial velocity and the exact solution is evaluated. The results of this test case are shown in Fig. 5, demonstrating that the expected orders of accuracy are recovered.

3.8.2. Constant density energy conservation

It has already been shown that mass and momentum conservation are obtained in the case of periodic boundary conditions. Furthermore, it has been shown that the kinetic energy in the system even for non-uniform meshes should be discretely conserved as long as the continuity equation is satisfied. In order to verify this for the presented scheme, a three-dimensional computation is performed in a unit box discretized on a 16^3 mesh, stretched in a similar way as for the vortex convection problem. The velocity field is initialized with uniform random numbers between -1 and 1, and projected to satisfy the divergence-free constraint. The time step size is set to $\Delta t = 0.002$. The evolution of the kinetic energy in the system is shown for two different time integration schemes, namely a second order explicit Runge–Kutta scheme and the semi-implicit second order Crank–Nicolson scheme presented in Section 3.6. Fig. 6 shows that the Crank–Nicolson scheme conserves kinetic energy, as expected. Interestingly, it can be observed that the higher the spatial order of accuracy, the faster the energy growth in time for the case of the second order Runge–Kutta scheme. As the spatial discretization already conserves kinetic energy, it appears important to use a time discretization that preserves this property to ensure a correct long time behavior of the solution even for high orders of accuracy. As a consequence, the Crank–Nicolson time advancement will be used in all the following test cases.

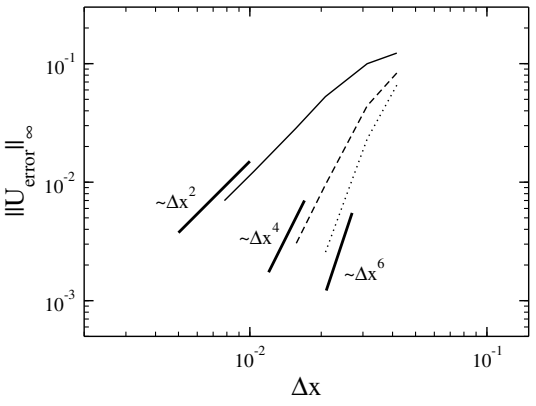

Fig. 5. Accuracy check for the inviscid convection of a circular vortex: second order (solid line); fourth order (dashed line); sixth order (dotted line).

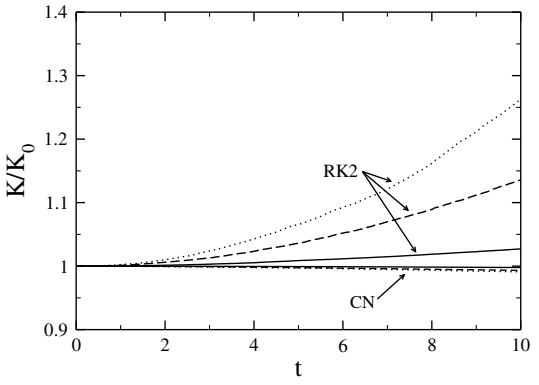

Fig. 6. Temporal evolution of the kinetic energy in the case of constant density: second order (solid line); fourth order (dashed line); sixth order (dotted line).

3.8.3. Variable density energy conservation

The discrete conservation of kinetic energy should also be satisfied even in the case of variable density. To verify this property, additional computations are performed in a unit box discretized on a 32^3 mesh. A turbulent velocity field with a Taylor microscale Reynolds number of about 33 is achieved by a linear forcing procedure [29]. The initial eddy turn-over time is $\tau_0 = 6.1$. A mixture fraction (Z) scalar field is initialized between 0 and 1 according to the procedure proposed by Eswaran and Pope [30]. Finally the density field is computed from the mixture fraction field using an equation of state corresponding to two miscible fluids

$$\rho(Z) = \frac{1}{aZ + b}. \tag{28}$$

The simulations were performed with a density ratio of 10 ($a = 9$, $b = 1$), a second order discretization for the convective and viscous part of the momentum equation, and a fifth order WENO scheme for the scalar transport equation. This first simulation is performed with both kinematic viscosity and diffusivity kept constant ($\mathrm{Pr} = 1$). Fig. 7 shows the time evolution of the kinetic energy in the domain. As expected, the kinetic energy follows a power law decay in time. The computation is restarted from $t = 5$ without viscosity and diffusivity to characterize the conservation properties of the different spatial discretizations. The variation in the total kinetic energy shown in Fig. 7(a) and (b) is small when compared to its decay in the presence of viscosity and diffusivity. The remaining variations may come from two contributions, namely the time integration errors or the pressure-dilatation term. In the latter case, the difference should correspond to an energy exchange with the internal energy. To quantify this energy transfer, an additional equation for the total internal energy is solved by

$$\frac{\mathrm{d}E_{\mathrm{int}}}{\mathrm{d}t} = p\nabla \cdot \mathbf{u}, \tag{29}$$

and the resulting reconstructed change in internal energy is presented in Fig. 7(c). As observed in Fig. 7(d), the total energy defined as the sum of kinetic energy (K) and internal energy (E_{int}) is nearly constant throughout the simulations for the three orders of accuracy (second, fourth, and sixth) tested. It can thus be inferred that the contribution from the temporal errors is very small, and that most of the kinetic energy variation can be explained by the effect of the pressure-dilatation term.

However, in this particular case, the pressure dilatation term arises only in the discrete equations. Indeed, in the absence of scalar diffusion, the scalar transport equation reads

$$\frac{\partial \rho Z}{\partial t} + \nabla \cdot (\rho \mathbf{u} Z) = 0. \tag{30}$$

Together with the continuity equation (Eq. (1)) and the equation of state (Eq. (28)), one can show that

$$\nabla \cdot \mathbf{u} = 0. \tag{31}$$

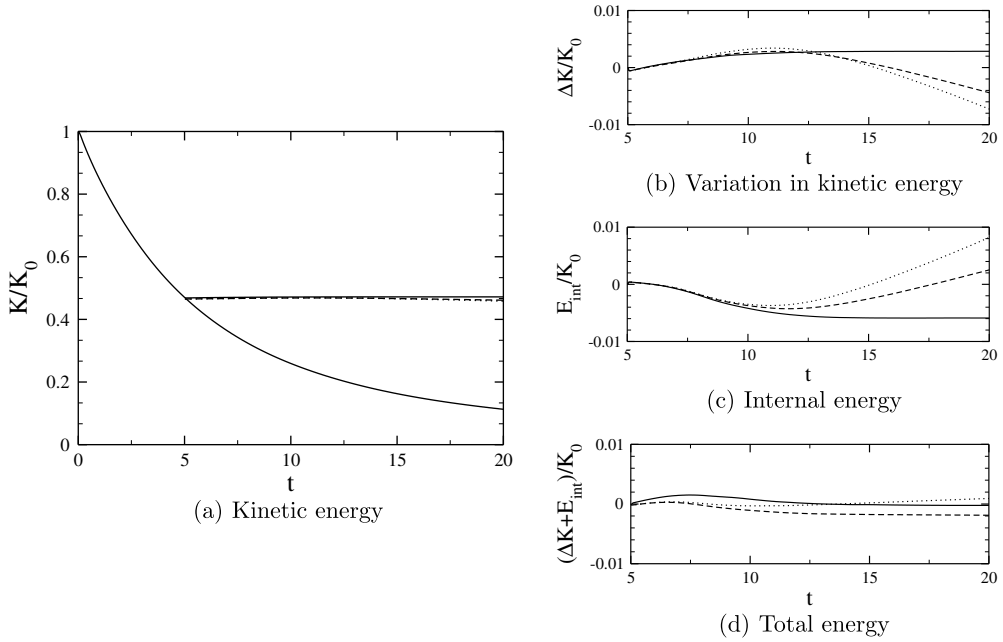

Fig. 7. Temporal evolution of the kinetic and internal energies in the case of variable density: second order (solid line); fourth order (dashed line); sixth order (dotted line).

As a result, under these circumstances, the total kinetic energy should remain constant and there should be no energy transfer to internal energy through the pressure-dilatation term. Nevertheless, as the discrete forms of the continuity equation and the scalar transport equation are different, Eq. (31) will not be satisfied discretely. This discrete discrepancy comes from using different operators for the divergence in the continuity and scalar transport equations, as well as different operators for the interpolation of the scalar and the density. This can be observed in the fact that the transfer to internal energy is larger for sixth and fourth order than it is for second order, as the discrete divergence operators corresponding to these orders of accuracy differ more strongly from the second order divergence operator used in conjunction with WENO-5. As a result, to limit the contribution from this spurious heat release, one should choose the scalar transport scheme such that the same divergence operator is used for the continuity and for the scalar transport equation. This conclusion could suggest that full finite difference schemes (such as $\mathrm{HOUC}^n_{\mathrm{FD}}$) are better suited for high order variable density simulations. However, as presented in Table 1, their global stencil size is larger, and it is more challenging to achieve boundedness of the scalar with such schemes. Considering that the spurious heat release observed in this case is very small, schemes such as third and fifth order WENO and $\mathrm{HOUC}^n_{\mathrm{FV}}$ will be preferred.

4. Boundary conditions treatment

4.1. Global conservation

In the case of non-periodic boundary conditions, local conservation does not imply global conservation, and therefore global conservation properties need to be redefined. With local conservation already satisfied, Morinishi et al. [15] defined global conservation through the relation

$$\sum_{k=1,}^{N_i} (h_i)_k \left.\frac{\delta\phi}{\delta x_i}\right|_k = \phi_{N_i+1/2} - \phi_{1/2}, \tag{32}$$

where N_i is the number of points in the ith direction. This property is the discrete equivalent to Green's theorem, and this condition is the basis of the boundary condition treatment proposed here.

Only boundary conditions corresponding to walls (slip and no-slip) as well as other Dirichlet conditions, such as inflow and convective outflow conditions [31,9], are treated in this paper. The different operators for interpolation and differentiation will be modified to account for boundaries in such a way that quantities outside the physical domain are never used. Primary conservation of mass and momentum will be discussed next.

4.2. Mass conservation

In a low-Mach number formulation, the pressure field is computed as the solution of a Poisson equation. The best boundary condition for the pressure is the application of zero normal gradients [32]. As a consequence, the volumetric integral of the pressure Laplacian is analytically zero

$$\int_V \Delta P \, \mathrm{d}V = \oint_{\delta V} \nabla P \cdot \mathrm{d}\mathbf{S} = 0. \tag{33}$$

To ensure that the equation solved for the pressure has a solution, its right hand side should verify the same condition. For instance, in a fractional step formulation, the Poisson equation is

$$\Delta(\delta P) = \frac{1}{\Delta t}(\text{cont-}n). \tag{34}$$

As a consequence, the volumetric integral of the continuity equation has to be analytically zero. The discrete form of this condition,

$$\sum_{x_1,x_2,x_3} J(\text{cont-}n) = 0, \tag{35}$$

ensures global mass conservation and is mandatory for low-Mach number formulations. This aspect is fundamental: if Eq. (35) is not satisfied, the Poisson equation for the pressure has no mathematical solution, since its right hand side is not in the image of the Laplacian operator. This and Eq. (32) define the necessary conditions that the divergence operator of the continuity equation has to satisfy.

While these properties are inherent to the second order formulation, a special treatment has to be derived for higher order formulations. As long as a divergence operator requires a velocity value outside the domain, Eq. (32) is not satisfied. For instance, a fourth-order divergence operator requires information about one point outside the domain and a sixth order formulation requires two values, which is shown in Fig. 8. To alleviate the problem arising in the fourth order formulation, Morinishi et al. [18] have proposed to compute the value for this outside point by using linear extrapolation with points inside the

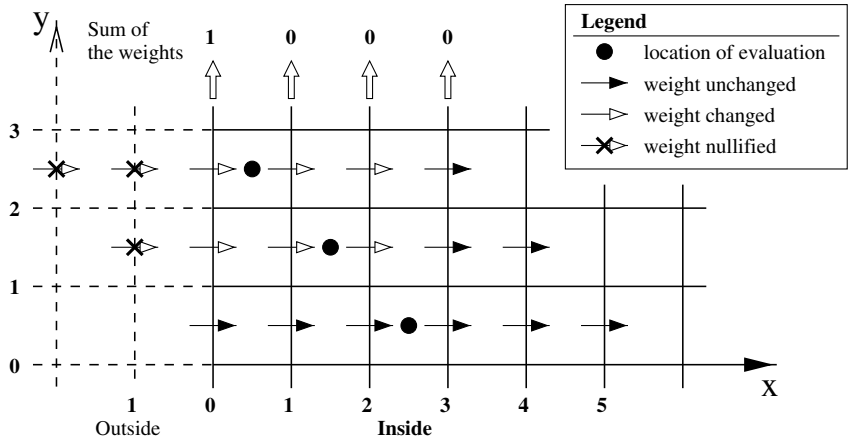

Fig. 8. Definition of the procedure to update the divergence operator to ensure mass conservation (illustrated for sixth order).

domain. They have shown that this discretely conserves mass. However, this approach cannot be easily extended to order higher than four.

In this paper, we propose a more general approach which can be derived for any order of accuracy. The differentiation operator given by Eq. (18) is expressed as a weighted linear combination of values at different grid points. In fact, Eq. (32) states that these weights add up to zero at every grid point in the domain except for the boundaries where their sums are either equal to $+1$ or -1, as shown in Fig. 8. This condition alone ensures discrete mass conservation.

Following this observation, the weights of the divergence operator corresponding to points outside the domain will be nullified, while the weights inside the domain will be adjusted to verify Eq. (32). Fig. 8 illustrates this procedure for the case of sixth order. If n is the order of the formulation, one can show that $n/2$ weights would have to be changed for $n/2-1$ divergence operators. As the condition derived from Eq. (32) only specifies $n/2$ independent constraints (one for each grid point), the determination of the updated weights is not unique. The weights are then chosen so as to optimize the order of accuracy of the divergence operators. This method is applied in such a way that the order of accuracy of the gradient normal to the wall increases with distance to the wall. The weights for the divergence operator have been precomputed for fourth and sixth order discretization and are available in Table 2 with the order of accuracy corresponding to the evaluation of the different quantities. Only the case of a boundary on one side is presented. It is straightforward to derive the divergence operators for the other side. It should be observed that in the case of fourth order discretization, the current procedure recovers the result proposed by Morinishi et al. [18].

As the normal velocity at a wall is zero, Eq. (35) is already satisfied. In the case of inflow/outflow conditions, the total mass flux leaving the domain should be exactly equal to the total mass flux entering the domain. For example, this could be done by adjusting the mean velocity at the outlet before solving the Poisson equation [33].

4.3. Momentum conservation

While global mass conservation is mandatory for low-Mach number formulations, global conservation of momentum might be relaxed. In fact, one might just use a simple procedure where velocities outside the domain are set to zero in the case of walls and to their corresponding values in case of inflow/outflow Dirichlet conditions. However, this procedure would not be very accurate. Furthermore, if exact conservation of momentum is preferred, a new procedure has to be derived. Morinishi et al. [15] proposed a method that discretely conserves momentum for fourth order accurate formulations by prescribing the flux at the single point outside of the physical domain. However, this approach cannot be easily extended to higher than fourth order, as different evaluations of the fluxes are required at the same point for higher order schemes.

To ensure that Eq. (32) is verified, the divergence and interpolation operators that appear in the momentum equation (Eq. (2)) have to be changed. The procedure will be outlined for the fourth order accurate discretization of the term $\mathrm{d}(\rho u_x u_y)/\mathrm{d}x$ for the u_y velocity component (Fig. 9). A similar procedure would be used for the treatment of the other convective terms. In the discretization of the momentum equation (Eq. (16)), the fluxes are constructed as the product of a full order interpolation of the momentum ($\overline{(\frac{J}{h_x}g_x)}^{4\mathrm{th}\zeta_y}$) and a second order interpolation of the velocities with variable stencil sizes ($\overline{u_y}^{(2l-1)\zeta_x}$). The procedure to ensure global conservation of momentum can be decomposed as follows:

Table 2
Weights for the mass conserving nth order interpolations

n	Weights								Effective order
	Outside		Inside						
4	–	0	$-\alpha_1-\frac{2}{3}\alpha_2$	$\alpha_1+\frac{1}{3}\alpha_2$	$\frac{1}{3}\alpha_2$	–	–	–	1
4	–	–	$-\frac{1}{3}\alpha_2$	$-\alpha_1$	α_1	$\frac{1}{3}\alpha_2$	–	–	4
6	0	0	$-\alpha_1-\frac{2}{3}\alpha_2-\frac{1}{5}\alpha_3$	$\alpha_1+\frac{1}{3}\alpha_2-\frac{2}{5}\alpha_3$	$\frac{1}{3}\alpha_2+\frac{2}{5}\alpha_3$	$\frac{1}{5}\alpha_3$	–	–	1
6	–	0	$-\frac{1}{3}\alpha_2-\frac{3}{5}\alpha_3$	$-\alpha_1+\frac{3}{5}\alpha_3$	$\alpha_1-\frac{1}{5}\alpha_3$	$\frac{1}{3}\alpha_2$	$\frac{1}{5}\alpha_3$	–	2
6	–	–	$-\frac{1}{5}\alpha_3$	$-\frac{1}{3}\alpha_2$	$-\alpha_1$	α_1	$\frac{1}{3}\alpha_2$	$\frac{1}{3}\alpha_3$	6

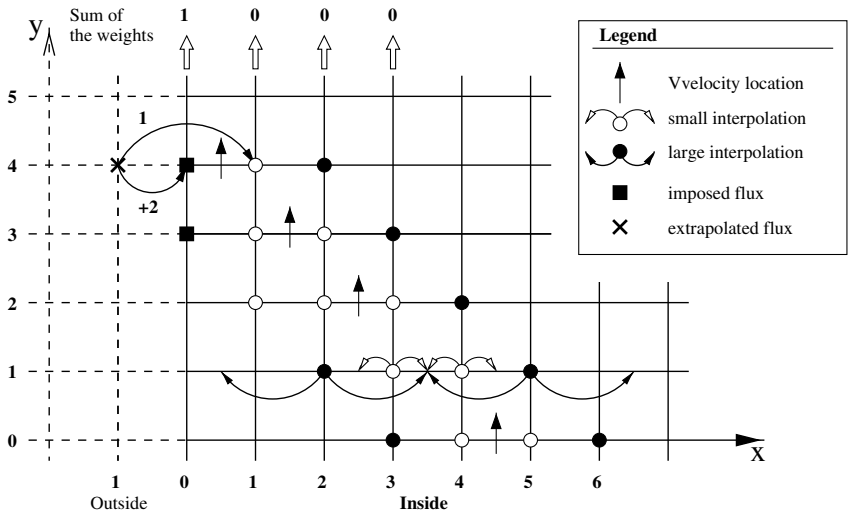

Fig. 9. Definition of the procedure to update the divergence operator to ensure momentum conservation (illustrated for fourth order).

- First, the size of the stencil used for the second order interpolations is changed as to avoid looking for a value outside of the physical domain. In Fig. 9, this is done for the flux evaluated at the point $(x, y) = (1, 2)$ for which the interpolation $\overline{u_y}^{3\zeta_x}$ is replaced by $\overline{u_y}^{1\zeta_x}$.
- Second, the momentum values used in the interpolation are set to zero for values outside the physical domain, as the normal velocity to the wall is always zero.
- Finally, the fluxes outside the domain are evaluated using second order extrapolation from values at the wall and inside the domain. For instance, the flux at the point $(x, y) = (-1, 4)$ would be written as

$$f|_{(-1,4)} = 2 \cdot \overline{\left(\frac{J}{h_x} g_x\right)}^{n\text{th}\zeta_y}\Bigg|_{(0,4)} \cdot u_y^{bc} - \overline{\left(\frac{J}{h_x} g_x\right)}^{n\text{th}\zeta_y}\Bigg|_{(1,4)} \cdot \overline{u_y}^{1\zeta_x}\Big|_{(1,4)}, \tag{36}$$

where u_y^{bc} would be zero for a wall.

The treatment of the pressure gradient is simpler because of its linear nature. In fact, the same procedure previously proposed for the divergence operator of the continuity equation is applied to the differentiation operator used for the pressure gradient (Table 2). Furthermore, a zero normal pressure gradient is enforced when evaluated at the boundary interface.

4.4. Energy conservation in an inviscid channel

The proposed boundary conditions were developed to ensure exact primary conservation (mass and momentum). To analyze their impact on the conservation of energy, the simulation of Section 3.8.2 is repeated with no-slip walls in the y direction. The same stretched mesh is used for the simulation. Fig. 10 compares the temporal evolution of the total kinetic energy for different orders of accuracy. The second order formulation recovers the energy conservation obtained in Section 3.8.2. On the other hand, the total kinetic energy increases for the fourth and sixth order formulations. However, this energy increase remains limited, and is found to be of the same order than the second order temporal errors obtained in Fig. 6 with the Runge–Kutta time integration scheme. Furthermore, in the presence of viscosity, the velocities at the wall would be zero, thus reducing even further the energy increase due to the proposed boundary treatment. In realistic configurations, such an increase in kinetic energy is expected to have very little effect on the overall solution, as will be shown for several wall-bounded flows in Section 7.

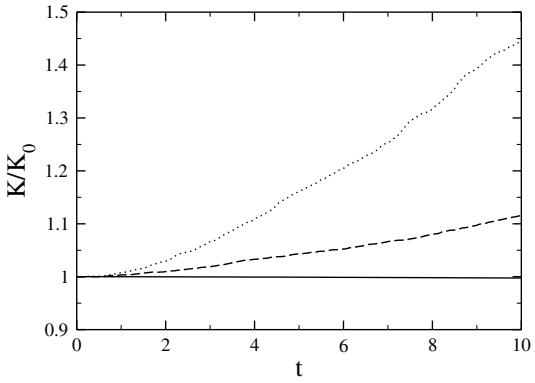

Fig. 10. Temporal evolution of the kinetic energy for a domain with walls: second order (solid line); fourth order (dashed line); sixth order (dotted line).

5. Centerline treatment

5.1. Singularity at the axis

In cylindrical coordinates, the Navier–Stokes equations present a singularity at the axis ($r = 0$) as the inverse of the radius appears in some of the terms of the continuity and momentum equations. Morinishi et al. [18] have already shown that this singularity is not physical, but rather originates from the coordinate system. For instance, the equation for the radial component of the velocity on the axis can be transformed to remove the singularity. For an inviscid flow, this would yield:

$$\frac{\partial \rho u_r}{\partial t} + \frac{\partial \rho u_x u_r}{\partial x} + \frac{\partial}{\partial r}\left(2\rho u_r u_r + \frac{\partial \rho u_r u_\theta}{\partial \theta} - \rho u_\theta u_\theta\right) + \frac{\partial p}{\partial r} = 0. \tag{37}$$

Furthermore, because of the coordinate transformation, the evaluation at the axis of some of the quantities is single-valued, while others are multi-valued. For example, the radial and azimuthal velocities are multi-valued at the axis since

$$u_r(x, 0, \theta) = u_y(x, 0)\cos\theta + u_z(x, 0)\sin\theta, \tag{38}$$

$$u_\theta(x, 0, \theta) = -u_y(x, 0)\sin\theta + u_z(x, 0)\cos\theta, \tag{39}$$

where u_y and u_z represent the two components of the velocity vector in a cartesian frame of reference. Any discrete formulation should ensure that both equations are satisfied.

5.2. Radial velocity on the axis

Because of the staggering arrangement of the components of the velocity vector inherent to the discrete formulation presented in Section 3, only the radial velocity is located exactly on the axis. To avoid the resulting singularity, several treatments have been proposed where the radial velocity at the axis is reconstructed from some off-axis values of velocity components [34,35,18]. All of these treatments are based on an equation equivalent to Eq. (38) and assume that the multi-valued radial component of the velocity vector can be expressed as

$$u_r(x, 0, \theta_{k+1/2}) = \overline{u_y}(x, 0)\cos\theta_{k+1/2} + \overline{u_z}(x, 0)\sin\theta_{k+1/2}. \tag{40}$$

Several expressions have been formulated for $\overline{u_y}$ and $\overline{u_z}$ as averages over the θ direction of the radial velocity or the azimuthal velocity or a combination of both. As the value of the radial velocity at the axis only appears in the convective and the viscous terms of the equations for the radial velocity, the formulation proposed by Morinishi et al. [18] is retained:

$$\overline{u_y}(x,0) = \frac{2}{N_\theta}\sum_{k=0}^{N_\theta-1} u_r(x,r_1,\theta_{k+1/2})\cos\theta_{k+1/2}, \tag{41}$$

$$\overline{u_z}(x,0) = \frac{2}{N_\theta}\sum_{k=0}^{N_\theta-1} u_r(x,r_1,\theta_{k+1/2})\sin\theta_{k+1/2}, \tag{42}$$

where r_1 is the radius of the first off axis radial velocity. Using the series expansion at the axis proposed by Constantinescu and Lele [36] for the radial velocity, one can show that the velocity thus reconstructed is second order accurate in the radial direction. However, since the value for the velocity is obtained by interpolation of other velocities, strict conservation of energy cannot be shown. In fact, Morinishi et al. [18] have already shown that the kinetic energy increases for purely inviscid flows.

Recently, Morinishi et al. [18] have formulated a discrete equation for the radial velocity at the axis, which discretely conserves kinetic energy. As for the velocity reconstruction, this equation is also second order accurate in the radial direction.

5.3. On the other side of the axis

The original discrete formulation of the Navier–Stokes equations by Morinishi et al. [18] was only second order accurate in the radial direction. As for simple pipe or jet flows most velocity gradients are found in this direction, it is worth considering increasing the order of accuracy in this direction. However, as the order of accuracy increases, the length of the stencil increases, and more and more points on the other side of the axis will have to be used. The concept of using information on the other side of the axis was proposed in the context of second order schemes by Eggels et al. [34], and used also for example by Verzicco and Orlandi [12].

Constantinescu and Lele [36] have already shown that necessary values at negative radius can be expressed as simple functions of values found at positive radius. For instance, they pointed out that:

$$\begin{aligned} u_x(x,-r,\theta) &= u_x(x,r,\theta+\pi),\\ u_r(x,-r,\theta) &= -u_r(x,r,\theta+\pi),\\ u_\theta(x,-r,\theta) &= -u_\theta(x,r,\theta+\pi). \end{aligned} \tag{43}$$

In the discrete formulation presented in Section 3, other quantities are also required for points across the axis. Following the same methodology, one can show that the scaling factors as well as the Jacobian satisfy similar symmetry or anti-symmetry conditions:

$$\begin{aligned} h_x(x,-r,\theta) &= \Delta x = h_x(x,r,\theta+\pi),\\ h_r(x,-r,\theta) &= \Delta r = h_r(x,r,\theta+\pi),\\ h_\theta(x,-r,\theta) &= -r\Delta\theta = -h_\theta(x,r,\theta+\pi),\\ J(x,-r,\theta) &= -r\Delta r\Delta x\Delta\theta = -J(x,r,\theta+\pi). \end{aligned} \tag{44}$$

The last relation is different from the relation used by Morinishi et al. [18] in their derivation of the equation for the radial velocity at the axis, where the Jacobian was given as

$$J(x,-r,\theta) = J(x,r,\theta+\pi). \tag{45}$$

However, the expression for the Jacobian in Eq. (45) cannot be used for higher order formulations of the terms in the radial directions, as it would introduce numerical errors in the divergence of the velocity field close to the axis. This can be clearly illustrated with the example of a uniform flow of unity velocity magnitude characterized by

$$\begin{aligned} u_r(x,r,\theta) &= +\cos\theta,\\ u_\theta(x,r,\theta) &= -\sin\theta. \end{aligned} \tag{46}$$

With Eq. (44), the fourth order accurate evaluation of the continuity equation (Eq. (18)) at the center of the first off-axis cell $(x, r_{1/2}, \theta)$ takes the form

$$(\text{cont-}n\text{-antisym}) = \frac{1}{r_{1/2}}(\alpha_1 + \alpha_2 - 1 + \mathrm{O}(\Delta\theta^4))\cos\theta, \tag{47}$$

which is indeed fourth order accurate since $\alpha_1 + \alpha_2 = 1$ (Eq. (12)). On the other hand, with Eq. (45), the continuity equation becomes

$$(\text{cont-}n\text{-sym}) = \frac{1}{r_{1/2}}\left(\alpha_1 + \frac{\alpha_2}{3} - 1 + \mathrm{O}(\Delta\theta^4)\right)\cos\theta, \tag{48}$$

which introduces a constant error in the continuity equation.

5.4. Test case

To assess the stability and accuracy of the possible treatments of the axis as well as the higher order formulations, a Lamb vortex [37] is convected in a cylindrical configuration across the axis. This configuration, which corresponds to a dipole vortex inside a circle of unity radius surrounded by a potential flow, was first presented by Verzicco and Orlandi [12]. The two-dimensional configuration consists of a disk with radius $R = 2.5$ with an initial vortex centered around $(r, \theta) = (1, 0)$. For a vortex centered on the axis, the velocity components are given by the expressions

$$u_r = \begin{cases} U\left(C\frac{J_1(a_1 r)}{a_1 r} - 1\right)\cos\theta & \text{for } r < 1, \\ -\frac{U}{r^2}\cos\theta & \text{for } r > 1, \end{cases} \tag{49}$$

$$u_\theta = \begin{cases} U\left(1 - C\left(J_0(a_1 r) - \frac{J_1(a_1 r)}{a_1 r}\right)\right)\sin\theta & \text{for } r < 1, \\ -\frac{U}{r^2}\sin\theta & \text{for } r > 1, \end{cases} \tag{50}$$

where $C = \frac{2}{J_0(a_1)}$, with $J_0(r)$ and $J_1(r)$ the Bessel functions of the first kind and a_1 the first root of the Bessel function ($J_1(a_1) = 0$). The vortex advects itself at the speed U. The expressions for an off axis vortex can easily be derived.

A first simulation is performed on a uniform mesh with resolution $N_x \times N_r \times N_\theta = 1 \times 64 \times 64$ to assess the conservation properties as well as the overall accuracy of the schemes. The timestep used for those simulations is taken to be $\Delta t = 5 \times 10^{-4}$, which corresponds to a maximum convective CFL condition in the azimuthal direction of 0.48, and which is small enough to avoid temporal errors. Fig. 11 shows the time history of the kinetic energy in the domain for various pole treatments and scheme orders. As expected, the solution of the equation for the radial velocity at the axis proposed by Morinishi et al. [18] assures perfect discrete con-

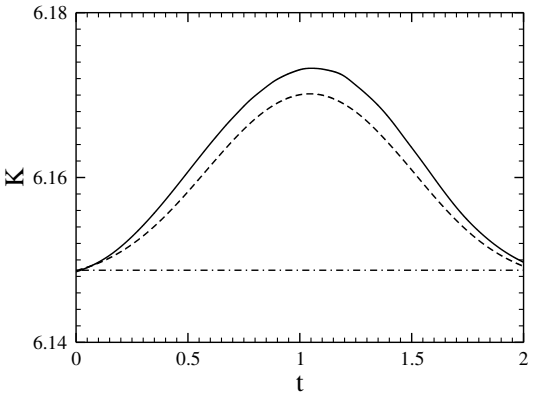

Fig. 11. Temporal evolution of the kinetic energy for the convection of a Lamb vortex for different pole treatments in cylindrical coordinates: second order (solid line) and fourth order (dashed line) with second order velocity reconstruction; second order with the axis equation of Morinishi et al. [18] (dash-dotted line).

servation of kinetic energy, while a reconstruction of the radial velocity by interpolation does not ensure strict conservation of kinetic energy. It is also to be noted that in this particular case, the kinetic energy fluctuations are smaller for higher order discretization. To better analyze the accuracy of the different pole treatments, contours of the vorticity magnitude are created as the vortex crosses the axis (Fig. 12). While the velocity reconstruction method does not conserve kinetic energy, it still shows good accuracy when compared to the exact solution. Increasing the order of accuracy leads to a small improvement of the results as the first order errors are mostly produced by the centerline treatment. The comparison has also been done for the pole treatment proposed by Morinishi et al. [18]. The solution of the discrete equation for the radial velocity at the axis introduces some disturbances upstream of the vortex and alter significantly the vorticity contours at the pole. By using a Taylor expansion in the radial direction, it can be shown that the discrete equation solved at the axis has the following limit:

$$\frac{\partial \rho u_r}{\partial t} + \frac{\partial \rho u_x u_r}{\partial x} + \frac{\partial}{\partial r}\left(\rho u_r u_r + \rho u_r \frac{\partial u_\theta}{\partial \theta} - \rho u_\theta u_\theta\right) + u_r \frac{\partial \rho u_r}{\partial r} + \frac{\partial p}{\partial r} = 0. \tag{51}$$

This equation differs significantly from Eq. (37) which should be the analytical equivalent for any equations for the radial velocity at the axis. These errors produced in a very small region of the domain might not affect the overall accuracy of the formulation in fully turbulent flows. However, it is preferable to ensure at least first order convergence everywhere in the domain in order to obtain that the numerical errors decrease with the mesh size. As a result, the choice was made to use the second order velocity reconstruction at the axis instead of enforcing strict energy conservation by solving the equation proposed by Morinishi et al. [18].

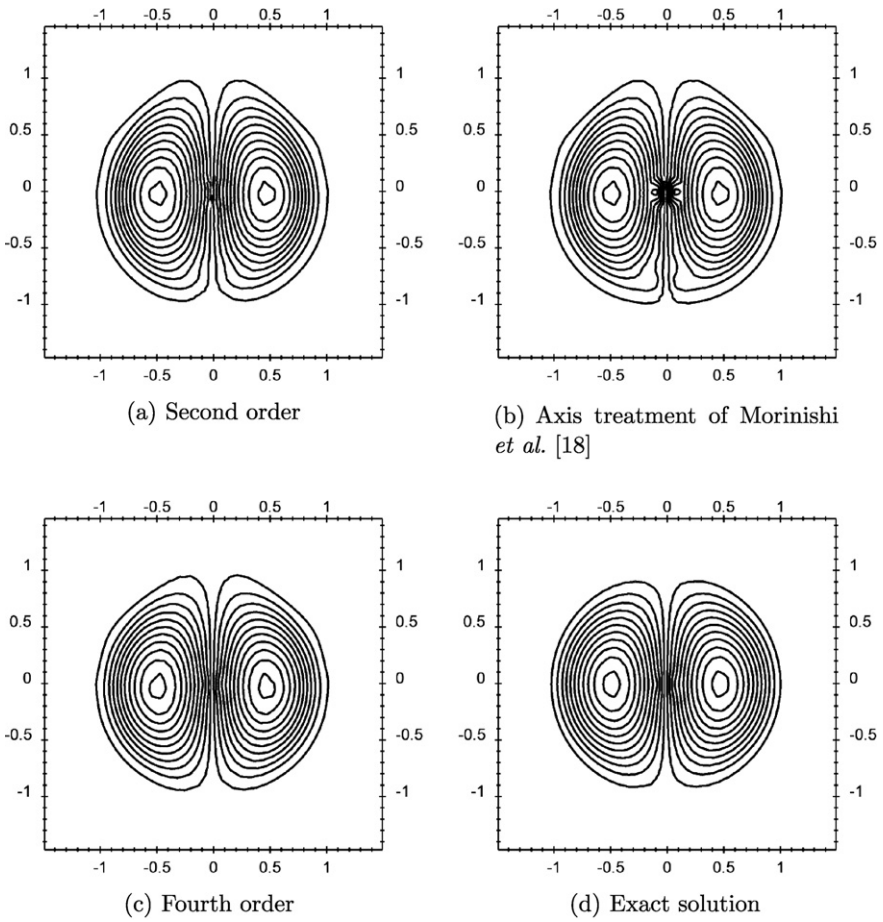

Fig. 12. Contours of vorticity magnitude for the convection of a Lamb vortex in cylindrical coordinates.

Finally a more thorough accuracy analysis has been performed by varying the mesh size. First, a solution is computed on a very fine mesh with $N_x \times N_r \times N_\theta = 1 \times 512 \times 512$. This solution is assumed to represent adequately the exact solution. Several runs are then performed with the second order accurate formulation with varying mesh sizes. Because of the semi-implicit nature of the time integration scheme, the computations are conducted with a maximum CFL condition in the azimuthal direction of 5. Fig. 13 shows the L_2 and L_∞ norms for the radial and the azimuthal velocities. Both norms for both components show nearly perfect second order accuracy for the simulation. Since the axis treatment is only second order accurate, and the test case puts the emphasis on the centerline itself, the higher order accurate formulations will not display better than second order accuracy. However, in realistic cases where the centerline does not play such a major role, we do not expect the limited accuracy at the axis to degrade the quality of the solution significantly, and therefore we should be able to fully benefit from the high order accuracy.

6. Viscous formulation

In order to consistently reduce the spatial discretization errors when solving the Navier–Stokes equations, the order of accuracy of the viscous terms should also be increased. However, no aliasing errors will be generated by these terms, since they are linear in velocity. Moreover, because of their dissipative nature, the viscous part of the Navier–Stokes equation does not typically lead to stability issues, and therefore it is more easily discretized than the convective part. Thus, a straightforward methodology for computing high order accurate viscous terms based on Lagrange polynomials will be presented here.

6.1. Numerical discretization

To consistently obtain high order accuracy on non-uniform meshes, we introduce a different set of discrete operators than for the convective terms, based on a local Lagrange polynomial representation of the quantity on which the operators have to be applied. In order to obtain an nth order accurate interpolation or differentiation of a quantity ϕ at a location x in the direction x_i, an $(n-1)$th order Lagrange polynomial P is fitted through the n data points available in the stencil. Note that this operation is centered in computational space, meaning that the interpolation or differentiation of ϕ is computed with as many stencil points on one side of the evaluation point than on the other. The interpolation is written

$$\bar{\phi}^{n\text{th}x_i} = P(x), \tag{52}$$

while the differentiation is expressed by

$$\frac{\delta_{n\text{th}}\phi}{\delta_{n\text{th}}x_i} = P'(x). \tag{53}$$

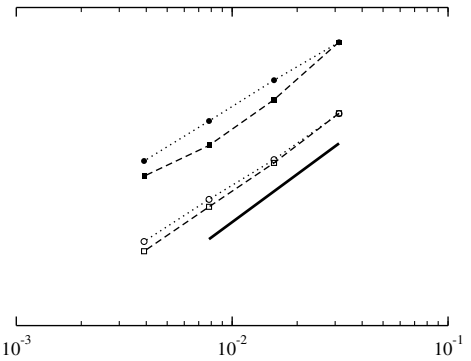

Note that we use the physical space in the notations, to differentiate these operators from the convective operators. Since all calculations are performed in physical space directly, high order accuracy is ensured even on non-uniform meshes. Note that these operators are all linear in ϕ, meaning that they can be pre-computed initially and stored at every mesh location in order to save computational time. With these operators defined, the divergence of the velocity vector based on the viscous metrics can be introduced as

$$(\text{visc-div-}n) = \frac{\delta_{n\text{th}} u_1}{\delta_{n\text{th}} x_1} + \frac{1}{\beta}\frac{\delta_{n\text{th}}(\beta u_2)}{\delta_{n\text{th}} x_2} + \frac{1}{\beta}\frac{\delta_{n\text{th}} u_3}{\delta_{n\text{th}} x_3}, \tag{54}$$

where β is one in cartesian coordinates and x_2 in cylindrical coordinates. The viscous term in the Navier–Stokes equation is then written

$$\begin{aligned}(\text{visc-}n)_{x_1} = {} & \frac{\delta_{n\text{th}}}{\delta_{n\text{th}} x_1}\left[2\mu\left(\frac{\delta_{n\text{th}} u_1}{\delta_{n\text{th}} x_1} - \frac{1}{3}(\text{visc-div-}n)\right)\right] + \frac{1}{\beta}\frac{\delta_{n\text{th}}}{\delta_{n\text{th}} x_2}\left[\beta\overline{\mu}^{2\text{nd}x_1\,2\text{nd}x_2}\left(\frac{\delta_{n\text{th}} u_1}{\delta_{n\text{th}} x_2} + \frac{\delta_{n\text{th}} u_2}{\delta_{n\text{th}} x_1}\right)\right] \\ & + \frac{1}{\beta}\frac{\delta_{n\text{th}}}{\delta_{n\text{th}} x_3}\left[\overline{\mu}^{2\text{nd}x_1\,2\text{nd}x_3}\left(\frac{1}{\beta}\frac{\delta_{n\text{th}} u_1}{\delta_{n\text{th}} x_3} + \frac{\delta_{n\text{th}} u_3}{\delta_{n\text{th}} x_1}\right)\right],\end{aligned} \tag{55}$$

$$\begin{aligned}(\text{visc-}n)_{x_2} = {} & \frac{\delta_{n\text{th}}}{\delta_{n\text{th}} x_1}\left[\overline{\mu}^{2\text{nd}x_1\,2\text{nd}x_2}\left(\frac{\delta_{n\text{th}} u_2}{\delta_{n\text{th}} x_1} + \frac{\delta_{n\text{th}} u_1}{\delta_{n\text{th}} x_2}\right)\right] + \frac{1}{\beta}\frac{\delta_{n\text{th}}}{\delta_{n\text{th}} x_2}\left[2\beta\mu\left(\frac{\delta_{n\text{th}} u_2}{\delta_{n\text{th}} x_2} - \frac{1}{3}(\text{visc-div-}n)\right)\right] \\ & + \frac{1}{\beta}\frac{\delta_{n\text{th}}}{\delta_{n\text{th}} x_3}\left[\overline{\mu}^{2\text{nd}x_2\,2\text{nd}x_3}\left(\frac{1}{\beta}\frac{\delta_{n\text{th}} u_2}{\delta_{n\text{th}} x_3} + \frac{\delta_{n\text{th}} u_3}{\delta_{n\text{th}} x_2} - \epsilon\frac{1}{\beta}\overline{u_3}^{n\text{th}x_2}\right)\right] \\ & - \epsilon\frac{1}{\beta}\overline{\left[2\mu\left(\frac{1}{\beta}\frac{\delta_{n\text{th}} u_3}{\delta_{n\text{th}} x_3} - \frac{1}{3}(\text{visc-div-}n) + \epsilon\frac{1}{\beta}\overline{u_2}^{n\text{th}x_2}\right)\right]}^{n\text{th}x_2},\end{aligned} \tag{56}$$

$$\begin{aligned}(\text{visc-}n)_{x_3} = {} & \frac{\delta_{n\text{th}}}{\delta_{n\text{th}} x_1}\left[\overline{\mu}^{2\text{nd}x_1\,2\text{nd}x_3}\left(\frac{\delta_{n\text{th}} u_3}{\delta_{n\text{th}} x_1} + \frac{1}{\beta}\frac{\delta_{n\text{th}} u_1}{\delta_{n\text{th}} x_3}\right)\right] + \frac{1}{\beta}\frac{\delta_{n\text{th}}}{\delta_{n\text{th}} x_2}\left[\beta\overline{\mu}^{2\text{nd}x_2\,2\text{nd}x_3}\left(\frac{\delta_{n\text{th}} u_3}{\delta_{n\text{th}} x_2} + \frac{1}{\beta}\frac{\delta_{n\text{th}} u_2}{\delta_{n\text{th}} x_3} - \epsilon\frac{1}{\beta}\overline{u_3}^{n\text{th}x_2}\right)\right] \\ & + \frac{1}{\beta}\frac{\delta_{n\text{th}}}{\delta_{n\text{th}} x_3}\left[2\mu\left(\frac{1}{\beta}\frac{\delta_{n\text{th}} u_3}{\delta_{n\text{th}} x_3} - \frac{1}{3}(\text{visc-div-}n) + \epsilon\frac{1}{\beta}\overline{u_2}^{n\text{th}x_2}\right)\right] \\ & + \epsilon\frac{1}{\beta}\overline{\left[\beta\overline{\mu}^{2\text{nd}x_2\,2\text{nd}x_3}\left(\frac{\delta_{n\text{th}} u_3}{\delta_{n\text{th}} x_2} + \frac{1}{\beta}\frac{\delta_{n\text{th}} u_2}{\delta_{n\text{th}} x_3} - \epsilon\frac{1}{\beta}\overline{u_3}^{n\text{th}x_2}\right)\right]}^{n\text{th}x_2}.\end{aligned} \tag{57}$$

6.2. Centerline treatment

The β coefficient equals x_2 in cylindrical coordinates, meaning that a singularity arises in the discretization of the viscous term when $1/r$ is evaluated at the centerline. In Eq. (55), this is never the case, since $1/r$ always appears off-axis as a result of the staggered variable arrangement. Similarly, in Eq. (56) the situation does not arise because the u_r velocity at the axis is obtained through a different procedure, as explained in Section 5. On the other hand, in Eq. (57), $\frac{1}{r}\frac{\delta_{n\text{th}} u_r}{\delta_{n\text{th}}\theta} - \frac{1}{r}\overline{u_\theta}^{n\text{th}r}$ is evaluated twice on the axis. However, on the centerline, the u_r and u_θ velocity components are related by

$$\frac{1}{r}\frac{\partial u_r}{\partial\theta} = \frac{u_\theta}{r}, \tag{58}$$

meaning that

$$\frac{1}{r}\frac{\delta_{n\text{th}} u_r}{\delta_{n\text{th}}\theta} - \frac{1}{r}\overline{u_\theta}^{n\text{th}r} = 0. \tag{59}$$

With this property, the singularity at the centerline can thus be removed by ensuring that when $r = 0$, $1/\beta$ is set to zero explicitly.

6.3. Boundary conditions

The strategy that was chosen to handle viscous boundary conditions differs significantly from that of the convective terms. In order to maximize the order of accuracy close to the boundaries, the operators that were

introduced for the viscous terms are upwinded to ensure that no point outside the physical domain is reached. The overall strategy is therefore to discard all stencil points that are outside the physical domain, and to construct upwinded operators from a Lagrange polynomial of the highest possible order given the available stencil points. For instance, as illustrated in Fig. 14 for fourth order, the evaluation of the polynomials (Eqs. (52) and (53)) at the point $(x, y) = (0, 3)$ are using two values inside the domain in addition to the boundary value itself whenever available. This methodology allows for an optimal accuracy close to the boundary, while ensuring that no outside value is ever used, which greatly simplifies the implementation of three-dimensional complex walls.

6.4. Decay of a Taylor–Green vortex

In order to verify the correct behavior of the proposed scheme for the viscous terms of the Navier–Stokes equations, the viscous dissipation of a two-dimensional Taylor–Green vortex inside a periodic box of size 2π has been simulated. The initial velocity is given by

$$\mathbf{u}(x, y) = \begin{pmatrix} \cos(x)\sin(y) \\ -\sin(x)\cos(y) \end{pmatrix}. \tag{60}$$

The mesh is uniform in the y direction, but has stretching in the x direction. If x_0 is uniform in $[0, 2\pi]$, the mesh is defined as $x = x_0 + s_x \sin(x_0)$. The value of s_x is set to 0.5, leading to very strong stretching. The viscosity is set to $\nu = 1 \times 10^6$ to make sure that the numerical errors due to the convective terms are negligible in comparison to the viscous errors. In order to ensure that the numerical errors due to the time integration remain low, a time step size of $\Delta t = 5 \times 10^{-10}$ is chosen, leading to a viscous CFL number consistently below 0.2. The ratio Γ_N between the kinetic energy in the system at time $t = 5 \times 10^{-8}$ and the initial kinetic energy is compared to its analytical value Γ_A and the error is plotted in Fig. 15. Two different cases have been tested, namely the full viscous formulation presented in the beginning of Section 6, shown in Fig. 15(a), and a similar formulation where the definition of the divergence operator used in the continuity equation (Eq. (18)) has been modified to match the divergence operator used in Eq. (54), shown in Fig. 15(b).

While the modified formulation displays the expected order of accuracy, the formulation with the unmodified divergence remains second order accurate, although the errors are greatly reduced by increasing the order of accuracy. This second order error is introduced when the dilatational part of the velocity gradient tensor is

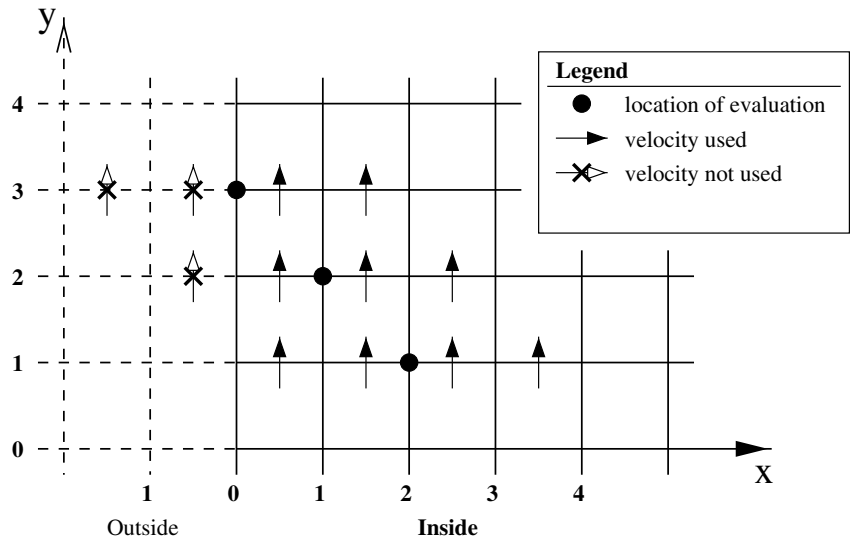

Fig. 14. Definition of the procedure to compute the differentiation/interpolation operators close to boundaries (illustrated for fourth order).

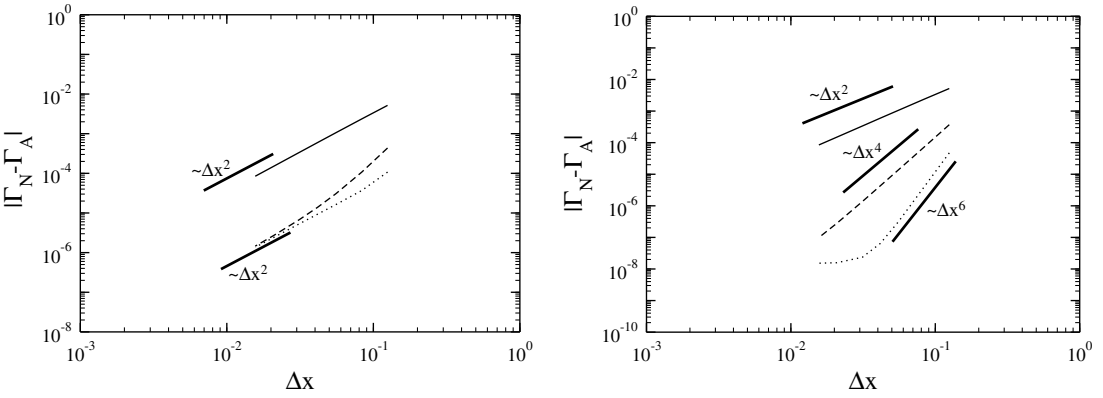

(a) (visc-div-n) from Eq. 54.

(b) $\sum_{i=1}^{3}\left(\frac{1}{J}\frac{\delta_{nth}}{\delta_{nth}\zeta_i}\left(\frac{J}{h_i}u_i\right)\right)$ replaced by (visc-div-n).

Fig. 15. Accuracy check for the viscous term for a Taylor–Green vortex flow: second order (solid line); fourth order (dashed line); sixth order (dotted line).

removed with a divergence operator that does not match the one used to enforce continuity. For an incompressible flow, we expect that $\nabla \cdot \mathbf{u} = 0$ discretely, however (visc-div-n) obtained by Eq. (54) will not be discretely zero. While this specific issue is interesting to notice, it is not expected to affect the quality of the results, since a significant reduction of two orders of magnitude is still obtained for the spatial discretization errors with the proposed formulation. Note also that in the absence of mesh stretching, the two divergence operators are discretely similar, therefore this problem does not arise.

7. Simulations of canonical flows

In this last section, the arbitrarily high order accurate methods presented before are employed to simulate a range of canonical flows. The focus is mainly to study the influence of the order of the numerical schemes on the solution. This influence will be evaluated by considering the classical quantities characterizing the flow statistics.

7.1. Homogeneous isotropic turbulence

For the first case, homogeneous isotropic turbulence is simulated by means of DNS and LES, conducted using the second, fourth, and sixth order schemes. The first simulation is for homogeneous isotropic turbulence forced linearly by the method proposed by Lundgren [29]. The Taylor Reynolds number is approximately 50, and the turbulence is resolved with $k_{\max}\eta > 1.5$, where $k_{\max}$ is the highest resolved wavenumber and η is the Kolmogorov scale, as suggested by Yeung and Pope [38]. Note that this is the DNS case 3c performed by Rosales and Meneveau [39]. Fig. 16(a) shows the nondimensional energy spectra obtained with the three numerical schemes used. It can be observed that for the three schemes the spectra are in excellent agreement with the results obtained by Rosales and Meneveau [39] with a spectral code. It seems however that the dispersive errors at the smallest resolved scale for the second order lead to a weak over-prediction of the energy at these scales. In the context of DNS, this does not appear to be a significant issue, since most of the energy dissipation occurs at larger scales.

The LES case is for decaying isotropic turbulence simulated on a 32^3 mesh using a classical dynamic sub-grid-scale model [41,42]. Note that for all the simulations in this paper, the evaluation of the velocity gradient tensor for the sub-grid scale model is performed with a second order accurate method, regardless of the order of accuracy used for the convective and viscous terms. The physical parameters are chosen to match the experiment of Comte-Bellot and Corrsin [40], and the initial field is constructed to have the three-dimensional energy spectrum of the experimental measurements at the first of the three measured

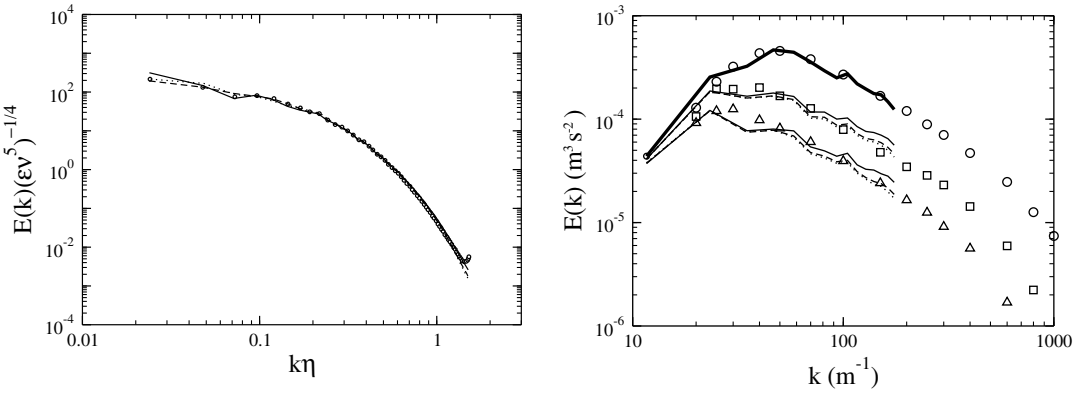

(a) DNS case (b) LES case

Fig. 16. Kinetic energy spectra for homogeneous isotropic turbulence simulations: second order (solid line); fourth order (dashed line); sixth order (dotted line); spectral simulation [39] (symbols in left figure); experimental spectra [40] (symbols in right figure); spectrum of initial field (thick line in right figure).

times. The energy spectrum at these three times is plotted in Fig. 16(b) for second, fourth, and sixth order. It can be observed that at the smallest resolved scales, which are much more energetic in the case of LES than for DNS, the numerical errors become noticeable. Indeed, the spectra in the second order case slightly over-predicts the energy on a significant part of the inertial sub-range. This would suggest that one should avoid using the second order accurate formulation for testing sub-grid scale models. These results are in agreement with the observations of Ghosal [43] and Chow and Moin [44]. Note that, even though there are noticeable differences between second and fourth order, results from sixth and fourth order are very close to each other. In our numerical experiments, we also observed that contributions from viscous and convective errors were of the same order.

7.2. Vortex ring colliding with a wall

To evaluate the impact of the proposed boundary conditions on the overall accuracy of the scheme, a vortex ring colliding with a wall is simulated. Following the numerical test of Verzicco and Orlandi [12], this simulation is performed in cylindrical coordinates using a two-dimensional axisymmetric domain of size $L_x \times L_r = 4 \times 4$, closed at $x = 0$ by a wall. Slip boundary conditions are applied at $x = 4$ and $r = 4$. A thin ring of initial Gaussian vorticity is placed at a height $x_0 = 2$ from the wall. The toroidal radius of the ring is set to $r_0 = 1$, leading to the following expression for the initial velocity field:

$$\mathbf{u}(x,r) = \begin{pmatrix} u_x \\ u_r \end{pmatrix} = \frac{1}{\pi s^2}\left(1 - \mathrm{e}^{-s^2/a^2}\right)\begin{pmatrix} r - r_0 \\ x_0 - x \end{pmatrix}, \tag{61}$$

where $s = \sqrt{(x - x_0)^2 + (r - r_0)^2}$ is the distance from the center of the ring core. As in [12], we set $a = 0.4131$ and the viscosity to 3.45×10^{-4}, leading to a Reynolds number of 2895. The simulation is run with a time step size $\Delta t = 0.03$ until $t = 30$, when the main vortex ring has generated both a secondary and a tertiary ring. The azimuthal vorticity contours are shown in Fig. 17 at the final time for second, fourth, and sixth order on a 128^2 mesh, as well as for second order on a 512^2 mesh. While the second order solution on the coarse mesh is already satisfactory, as pointed out by Verzicco and Orlandi [12], the solution converges towards the fine mesh solution as the order of accuracy is increased. To quantify this convergence, the azimuthal vorticity is plotted as a function of r at $x = 0.75$ for all four cases in Fig. 18. It clearly appears that the second order solution is not able to fully capture the peak in vorticity at $r = 2.75$, while the fourth order solution follows very accurately the fine mesh solution. Interestingly, very small differences are observed between the fourth order solution and the sixth order solution, indicating that for the given mesh, convergence in the order of the scheme has almost been achieved. It can be noted that it was observed for this case that the convective order of accu-

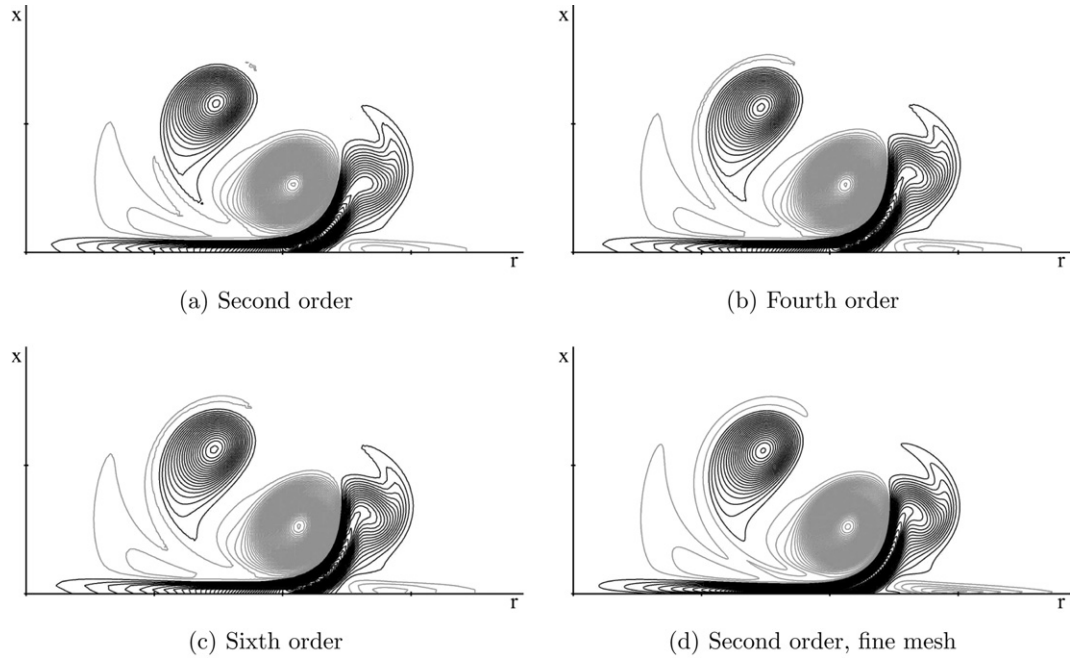

Fig. 17. Azimuthal vorticity contours of a vortex ring colliding with a wall at $t = 30$.

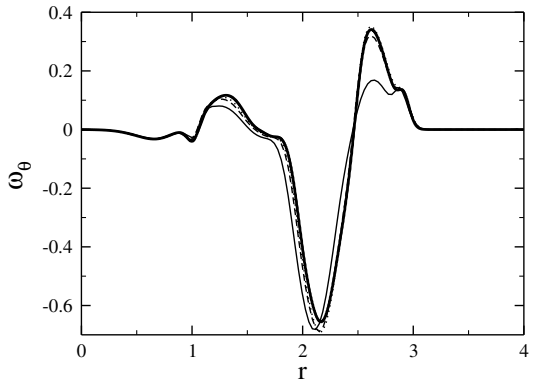

Fig. 18. Azimuthal vorticity as a function of r at $x = 0.75$ and $t = 30$: second order (solid line); fourth order (dashed line); sixth order (dotted line); second order on the fine mesh (thick line).

racy was the most important. In our numerical tests, little improvement was obtained by increasing the order of accuracy of the viscous term.

7.3. Rayleigh–Taylor instability

The two-dimensional Rayleigh–Taylor instability problem is considered to check the ability of the method to simulate variable density flows accurately. The configuration consists of two miscible fluids separated by a horizontal perturbed interface. The heavy fluid (with unity density) is above the light fluid (with density 0.1). The mean interface is located at $y = 0$ in a domain size of $[-0.5, 0.5] \times [-0.5, 0.5]$. The exact location of the interface is given by

$$y_{\text{int}}(x) = -\alpha \sum_{k=1}^{7} \cos(\omega_k \pi x), \tag{62}$$

where the amplitude of the sinusoidal waves is $\alpha = 0.001$ and the wave numbers are $\omega_k = 4, 14, 23, 28, 33, 42, 51, 59$, following the test case of Nourgaliev and Theofanous [22]. A mixture fraction scalar field is constructed as

$$Z(x,y) = \frac{1}{2}\left(1 + \tanh\left(\frac{y_{\text{int}}(x) - y}{2\delta}\right)\right), \tag{63}$$

where the thickness of the interface is $\delta = 0.002$. Finally, the density is evaluated from the mixture fraction using the same equation of state as previously used in Section 3.8.3. The two fluids have identical kinematic viscosity $\nu = 0.001$ and kinematic diffusivity $D_Z = 0.0005$. The value for the gravity acceleration is $g = 9$ so that the Reynolds number is $\text{Re} = \sqrt{gL_y}L_x/\nu = 3000$. Simulations have been performed on two different meshes. A coarse mesh of $N_x \times N_y = 128 \times 128$ has been used for simulations with second, fourth, and sixth order accurate formulations, while a solution has been obtained on a finer grid of $N_x \times N_y = 512 \times 512$ mesh points with the second order formulation. The time step size is $\Delta t = 0.001$ for the coarse mesh and $\Delta t = 0.00025$ for the fine mesh.

Fig. 19 shows the time evolution of the kinetic energy and the internal energy defined by Eq. (29) for the four simulations. While the fourth order formulation shows some differences compared to the second order, the sixth order shows little improvement over fourth order. As previously explained in Section 3.8.3, the energy transfer to internal energy is caused by the discrepancy between the continuity and scalar transport equations. In the present simulations, there are two reasons for this discrepancy. The first contribution has already been described and comes from the numerical discretization. It is grid dependent and its effect decreases as the grid is refined. The amplitude of this contribution can be assessed by comparing the internal energy on the coarse and on the fine mesh. The second contribution comes from the scalar diffusion term. It appears clear that the transfer to internal energy due to the numerical discretization is very small in comparison to the contribution due to the scalar diffusion.

Contour plots of the density are extracted at $t = 0.75$ for the four simulations (Fig. 20). While the second order formulation predicts the overall features of the instability, the fourth and sixth order formulations compare more favorably to the solution on the finer mesh. To further quantify these differences, the density profile at $y = 0$ is plotted in Fig. 21. The second order formulation, while capturing the overall shape of the density profile, is unable to correctly predict the dip in density at $x = \pm 0.1$. Increasing the order of accuracy from second to fourth and then to sixth leads to quantitatively better predictions of the density profile.

7.4. Turbulent pipe

To further analyze the influence of higher order discretization on turbulent simulations in the presence of mean gradients, a turbulent pipe flow is simulated by means of DNS. The configuration was originally investigated experimentally and numerically by Eggels et al. [34]. The Reynolds number, based on the radius and the friction velocity, was $\text{Re}_\tau = 180$ for the DNS and in the range $\text{Re}_\tau = 183$–190 for the experimental setup.

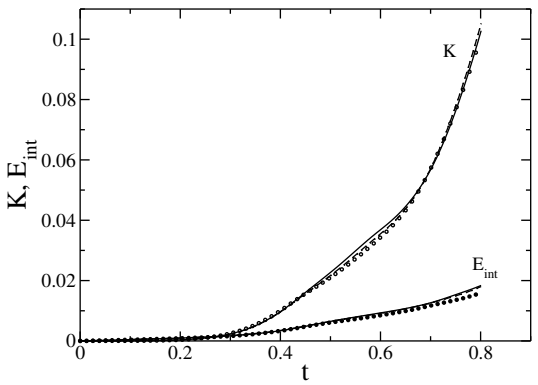

Fig. 19. Temporal evolution of kinetic and internal energies of the Rayleigh–Taylor instability: second order (solid line), fourth order (dashed line), and sixth order (dotted line); second order on the fine mesh (symbols).

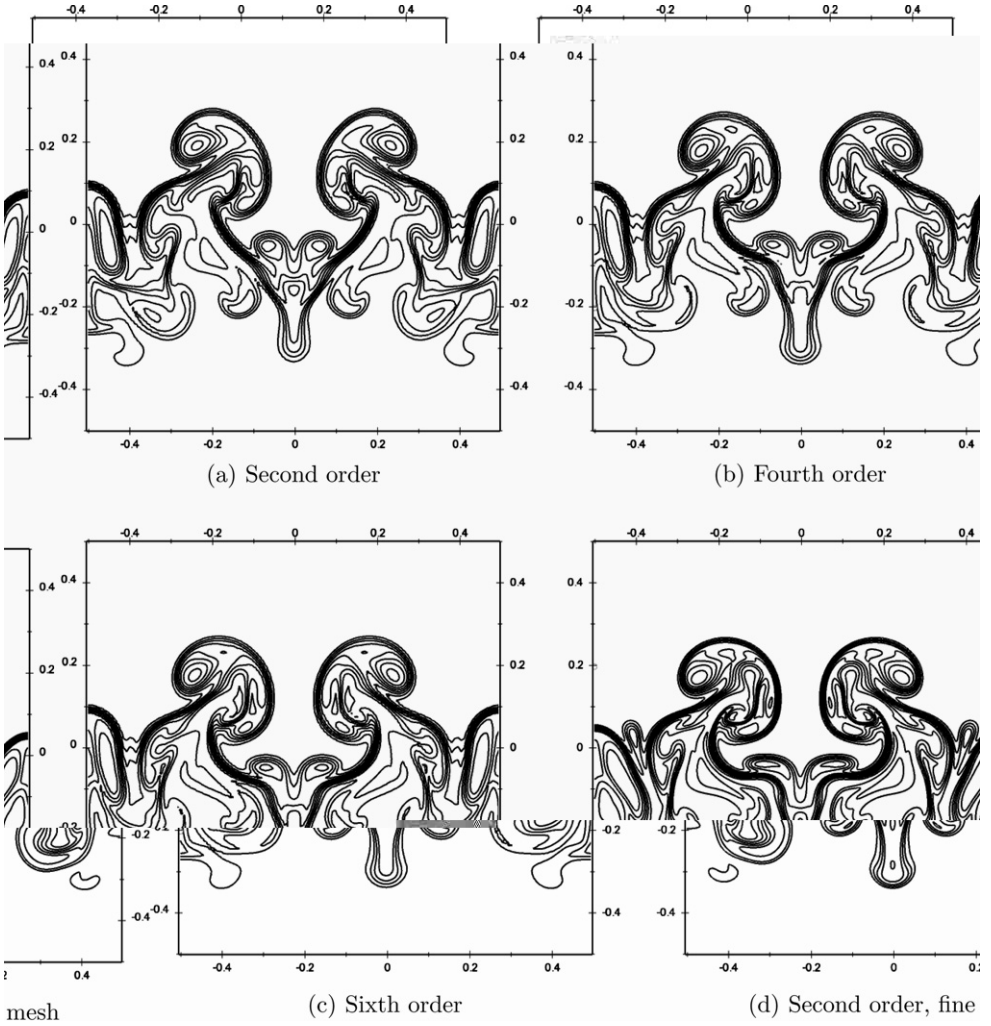

Fig. 20. Density contours of Rayleigh–Taylor instability at $t = 0.75$.

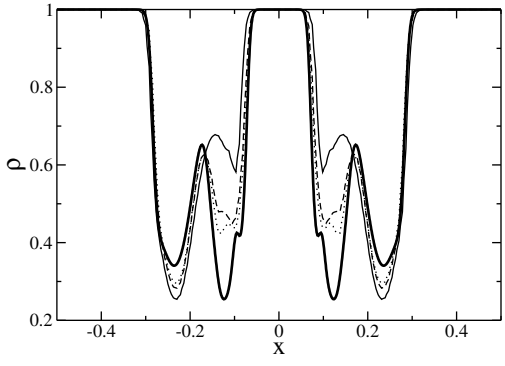

Fig. 21. Density as a function of x at $y = 0.20$ and $t = 0.75$: second order (solid line); fourth order (dashed line); sixth order (dotted line); second order on the fine mesh (thick line).

For the DNS, Eggels et al. [34] used a domain of size $L_x \times L_r \times L_\theta = 10R \times R \times 2\pi$ and a grid resolution of $N_x \times N_r \times N_\theta = 256 \times 96 \times 128$ points. Further numerical analysis has been performed by Fukagata and Kasagi [35] with the same grid resolution but a different numerical discretization. The same grid resolution has been used for the present simulations, but with different orders of accuracy. The results are compared with the latest DNS results by Fukagata and Kasagi [35] and the experimental measurements of Eggels et al. [34] in Fig. 22(a), (c) and (e).

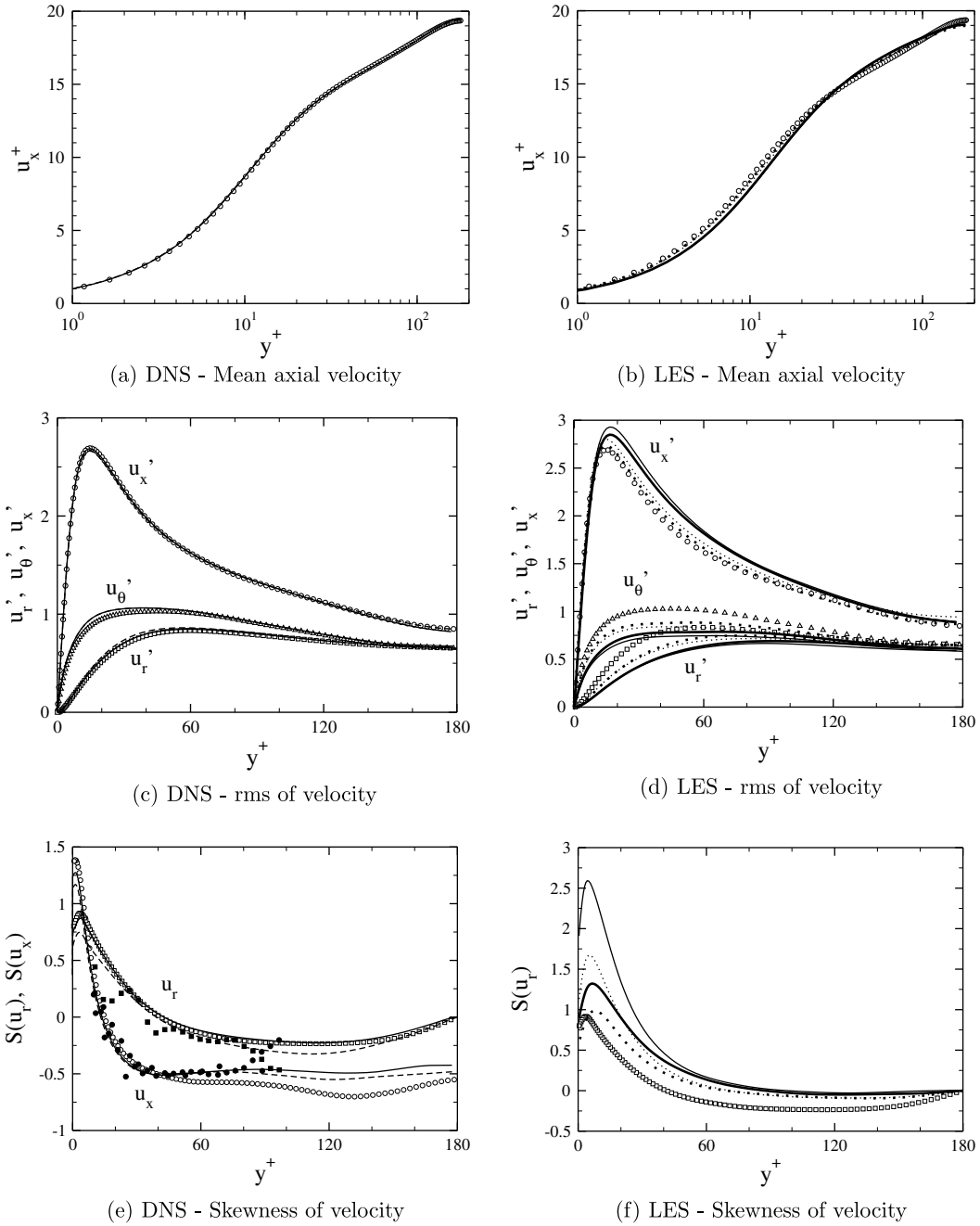

Fig. 22. Statistics of a pipe flow for the DNS and the LES cases: second order (solid line); fourth order (dashed line); sixth order (dotted line); DNS of Fukagata and Kasagi [35] (open symbols); experimental measurements of Eggels et al. [34] (closed symbols); dynamic Smagorinksy model (thin lines); Lagrangian dynamic model (thick lines).

The mean and the fluctuations of the velocities obtained with both the second and fourth order formulations compare extremely well with the DNS data of Fukagata and Kasagi [35]. The comparison of the fluctuations of the velocities shows only very little differences for the radial and azimuthal velocities. Also the skewness profiles of the radial and the axial velocities agree well with the experiments for the fourth order scheme, while the second order shows some minor deviations, especially in the viscous sub-layer where a slight over-prediction can be noticed. This over-prediction can also be observed in the second order accurate DNS results of Fukagata and Kasagi [35]. The skewness of the axial velocity in the log-layer is predicted to be nearly constant (around -0.5) by the second and fourth order formulations in agreement with the experimental measurements. On the other hand, the DNS data of Fukagata and Kasagi [35] predicts significantly lower values.

The importance of higher order accuracy is also investigated in the framework of LES. Because of the low Reynolds number, when simulated on a relatively coarse grid and with low order of accuracy, the flow can relaminarize [18]. Morinishi et al. [18] have already performed several simulations with different orders of accuracy for the convective terms in the axial and azimuthal directions. However, the convective term in the radial direction as well as all diffusion terms remained second order accurate. In the present work, we intend to analyze the effects of higher order formulations for all convective and viscous terms. Two LES (second order and sixth order accurate) were performed using the grid employed by Morinishi et al. [18] with a resolution of $N_x \times N_r \times N_\theta = 48 \times 64 \times 48$ points. Two sub-grid scale models have been tested, namely a standard dynamic Smagorinsky model [41,42] and the Lagrangian dynamic sub-grid scale model by Meneveau et al. [45].

Fig. 22(b), (d), and (f) show the results obtained for the four simulations performed in comparison with the DNS results of Fukagata and Kasagi [35]. As expected, the sixth order formulation predicts significantly more accurately the mean and fluctuations of the velocities. The skewness of the radial velocity is greatly improved by changing the order of accuracy from second to sixth order. These results clearly show that increasing the order of accuracy of the convective terms in the radial direction as well as all the viscous terms has a significant impact on the quality of the LES predictions. It should also be noted that the impact of changing the order of accuracy appears far greater than that of changing the sub-grid scale model. For the given mesh, the Lagrangian model was found to consistently predict the flow with better accuracy than the standard dynamic procedure [41,42]. However, the improvement that can be obtained by changing the sub-grid scale model is limited in comparison with the effect of increasing the order of accuracy of the numerical schemes, except for the skewness prediction, where the Lagrangian model performs surprisingly well. To analyze the performance of sub-grid scale models, the numerical errors due to the spatial discretization should be sufficiently small [43,44], therefore it appears that the second order formulation should not be used in this case to develop and analyze models.

7.5. Round jet

Finally, the higher order formulations are applied in an LES of a variable density turbulent jet (Fig. 23). The configuration, studied experimentally by Amielh et al. [46] and Djeridane et al. [47], corresponds to an axisymmetric jet at ambient pressure and temperature. Pure helium is injected through a pipe of diameter $D_j = 26$ mm at a bulk velocity of $\overline{U}_j = 25$ m/s. A slow surrounding co-flow of air is supplied at a bulk velocity of $U_e = 0.9$ m/s. The entire configuration is enclosed in a cylindrical vessel of internal diameter $D_e = 285$ mm. The Reynolds number based on the diameter of the helium pipe and the average velocity on the axis ($U_j = 32$ m/s) is $\mathrm{Re}_j = 6890$. The density ratio between helium and air is about 7.2. The LES is performed on a grid with a resolution of $N_x \times N_r \times N_\theta = 128 \times 76 \times 64$ points. The sub-grid scale model used for the current simulations is the Lagrangian dynamic subgrid-scale model by Meneveau et al. [45] and extended for variable density and to include the modeling of the turbulent eddy diffusivity by Réveillon and Vervisch [48]. The fluid properties, such as the molecular viscosity and the molecular diffusivity, as well as the equation of state, are precomputed and tabulated as a function of mixture fraction. In order to generate the inflow conditions, a periodic cylindrical pipe is first computed. The turbulent velocity field at an x position is stored as a function of time in order to be re-injected at the entrance of the jet simulation. The computations are performed using the second and fourth order accurate formulations, and compared to the experimental results

Fig. 23. Volumetric rendering of the mixture fraction of helium for the variable density jet.

in Fig. 24. The rms values of the velocities are non-dimensionalized by using the velocity on the axis (U_c). The radii are non-dimensionalized by using the velocity half width radius ($R_{1/2}$).

Fig. 24(a) shows that for both second and fourth order, the statistics at the first measurement station ($x/D_j = 0.2$) are in excellent agreement with the experimental results. The mean axial velocity on the axis shown in Fig. 24(b) is predicted with excellent accuracy as well as by both the second order and the fourth

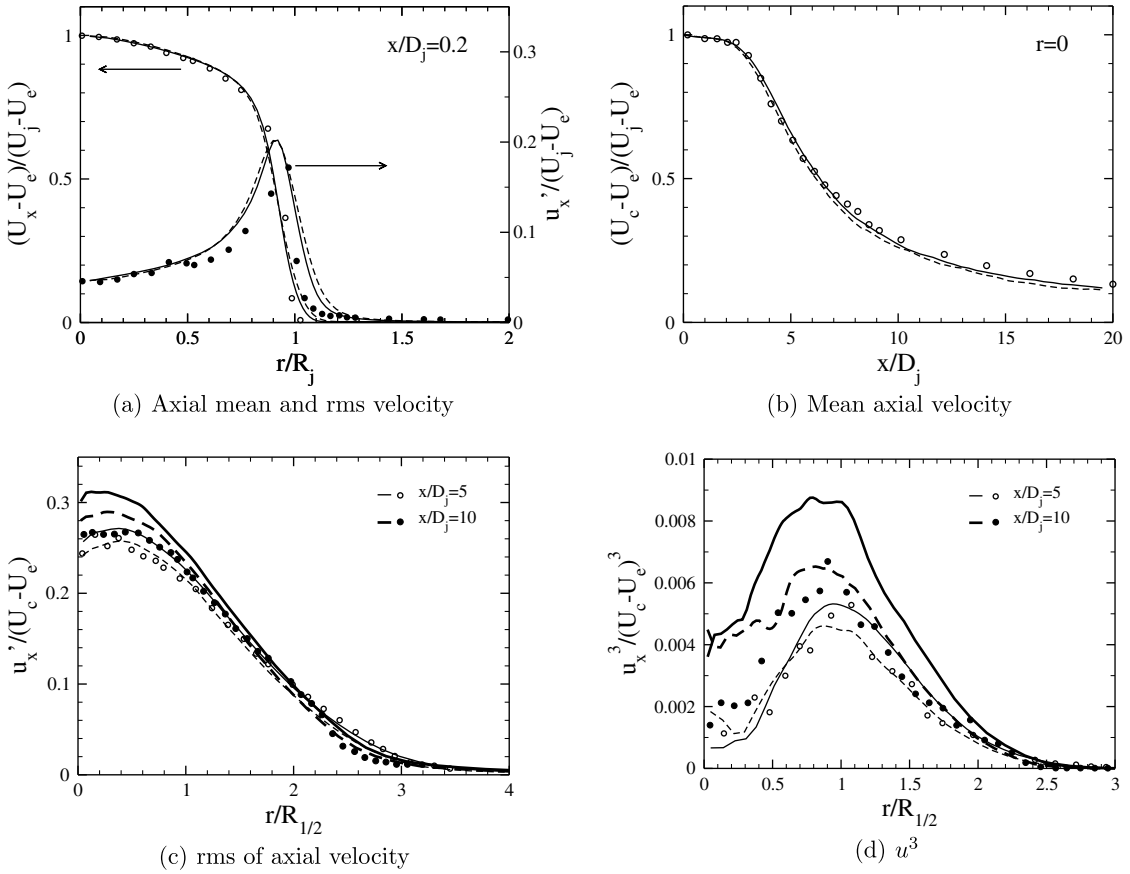

Fig. 24. Statistics of the LES of the turbulent variable density jet: second order (solid line); fourth order (dashed line); experimental measurements [47,46] (symbols).

order formulations. The length of the potential core as well as the decay of the mean velocity in the self similar region of the jet are well captured. However, differences between the two formulations start to appear when looking at higher order statistics. Fig. 24(c) shows the rms of the velocity at two locations in the jet at $x/D_j = 5$ and $x/D_j = 10$. The second order formulation consistently over-predicts the velocity rms close to the center of the jet, while the fourth order formulation performs slightly better. The same conclusion can be obtained by looking at the third order statistics shown in Fig. 24(d). Again, the second order formulation consistently leads to an over-prediction, while the fourth order results follow more accurately the experimental profiles. Overall, both the second and fourth order formulations predict with good accuracy the mean quantities. However, higher order statistics are better predicted with higher order formulations. It can be noted that the improvement obtained by increasing the order of accuracy is not as impressive as for the turbulent pipe case. This can be attributed to the use of a very coarse mesh, on which one can expect that the sub-grid scale modeling errors might be more dominant.

7.6. Cost

The improved accuracy that can be obtained by running with higher order schemes comes at a price: indeed, the size of the stencils involved in the computations is significantly increased, and therefore the number of operations is expected to increase as well when using higher order schemes. As a consequence, one may wonder what is most efficient: retaining a low order accurate scheme and increasing the size of the mesh, or increasing the accuracy of the numerical schemes. Clearly, this is a difficult question, for the answer will strongly depend on the problem considered. However, it is possible to investigate this issue for a few simple test cases, where the error and the cost can be properly evaluated.

First, it is interesting to report here the average cost per time step for some of the test cases presented before, using different orders of accuracy. Table 3 summarizes this information. On average, going from second to fourth order accuracy leads to doubling the cost of the simulation, while going from fourth to sixth order slightly less than doubles the simulation cost. Considering the improvement on the quality of the predictions that was observed for the different test cases, it appears that the fourth order accurate formulation could be very beneficial. For instance, in the case of the inviscid convection of a circular vortex presented in Section 3.8.1, one only has to use half the mesh points in each direction with the fourth order formulation to obtain the same error level as the second order scheme. At constant CFL, this would translate to a factor 4 reduction in CPU time for two-dimensional simulations and a factor 8 for three-dimensional simulations. A more rigorous assessment of this is shown in Fig. 25, where the L_∞ norm of the error between the computed axial velocity and the exact solution for various mesh sizes is plotted as a function of the cost for one time step, normalized by the cost of one time step on a 24×24 mesh with second order accuracy. This test clearly shows that there is a range of errors for which it is more efficient to use fourth order accuracy instead of second order accuracy. However, for most of the error range tested, sixth order accuracy is too expensive to be of interest, except if very small errors are necessary. These results are obviously for the considered case, but they suggest in general that for different ranges of errors, different schemes might be more efficient.

A more realistic problem is the LES of a turbulent pipe presented before. For this problem, the mesh has been varied, and the mean axial velocity is compared to DNS. Three meshes are considered, namely a $24 \times 32 \times 24$ mesh, a $32 \times 48 \times 32$ mesh, and a $48 \times 64 \times 48$ mesh. We are interested in comparing the

Table 3
Timing of different runs at various orders

Order	Turbulent pipe		Rayleigh–Taylor		Vortex ring		Isotropic turbulence	
	Time	Ratio	Time	Ratio	Time	Ratio	Time	Ratio
2	3.33	–	1.17	–	0.84	–	1.20	–
4	5.62	1.69	2.54	2.17	2.23	2.65	1.84	1.53
6	8.57	1.52	4.75	1.87	3.55	1.60	3.00	1.63

Times are per time step, in seconds.

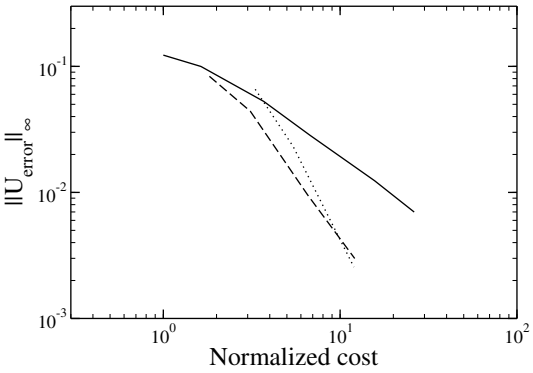

Fig. 25. Error as a function of cost per time step when increasing mesh size for the inviscid convection of a circular vortex: second order (solid line); fourth order (dashed line); sixth order (dotted line).

relative cost of increasing the mesh size or increasing the order of accuracy, as well as the quality of the predicted axial velocity profile. Fig. 26 shows the mean axial velocity with second order accuracy for the three different meshes, and the mean axial velocity for various orders of accuracy for the coarsest mesh. It is interesting to note that the fourth order results on the $24 \times 32 \times 24$ mesh are very similar to the second order results on a $32 \times 48 \times 32$ mesh. Table 4 shows the cost per time step of the different computations, as well as the relative errors between the LES mean axial velocity predictions and the DNS results at $y^+ = 10$. Here, it can be observed that the fourth order computation on the coarse mesh is about half

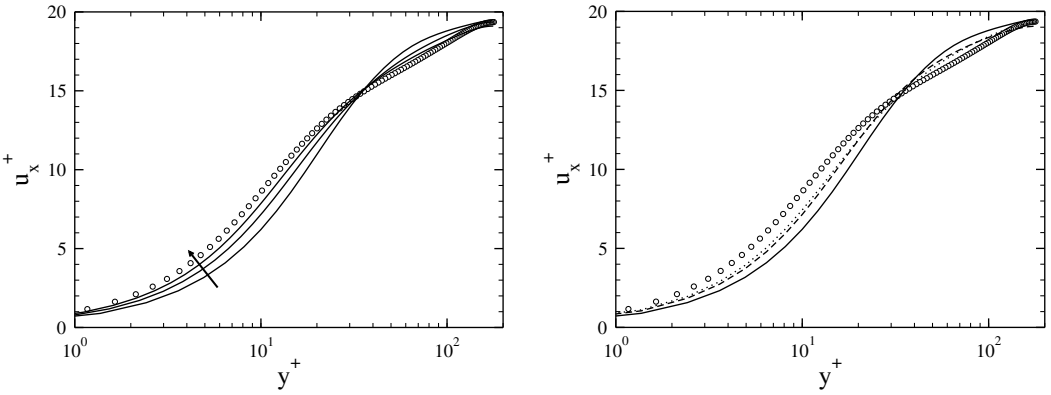

(a) Second order accuracy, increasing mesh size

(b) $24 \times 32 \times 24$ mesh, increasing order of accuracy

Fig. 26. Mean axial velocity for the LES of a pipe flow: second order (solid line); fourth order (dashed line); sixth order (dotted line); DNS of Fukagata and Kasagi [35] (open symbols); increasing mesh size is indicated by the arrow.

Table 4
Time per time steps, in seconds, and relative errors between LES and DNS at $y^+ = 10$, for different order of accuracy and different meshes for the turbulent pipe LES

Order	$24 \times 32 \times 24$		$32 \times 48 \times 32$		$48 \times 64 \times 48$	
	Cost	Error	Cost	Error	Cost	Error
2	0.230	0.278	0.627	0.166	2.120	0.085
4	0.358	0.169	0.989	0.097	3.184	0.030
6	0.517	0.135	1.453	0.089	4.456	0.026

the cost of the second order computation on the medium mesh, while these two simulations lead to similar errors. The same remark applies to the fourth order computation on the medium mesh compared to the second order computation on the fine mesh. Note also that these comparisons do not account for the fact that the time step size increases as the mesh is coarsened. Here again, the fourth order method seems beneficial for this case. However, the added cost of using the sixth order scheme is not justified by the increase in accuracy, which is very limited between fourth and sixth order. Indeed, it is expected that the LES modeling errors will very quickly dominate the computation, and that further improvement in the quality of the predictions will require first to improve the model.

8. Conclusion

A variable density, conservative, arbitrarily high order finite difference method has been presented and tested, that is an extension of the work of Morinishi et al. [18]. Discrete conservation properties as well as accuracy have been verified with variable density and non-uniform meshes, both for cartesian and cylindrical coordinates. For the sake of completeness, an arbitrarily high order formulation of the viscous terms of the Navier–Stokes equations has been proposed. A specific treatment of the boundary conditions is proposed that ensures discrete primary conservation, while secondary conservation remains highly satisfactory. Similarly, an analysis of the centerline behavior for high order schemes has been conducted that provides adequate behavior of the solution in cylindrical coordinates. The full approach allows for accurate, robust, and flexible simulations of turbulent reactive flows in complex geometries. This technique has been applied in a range of test problems, including laminar and turbulent flows, constant and variable density flows, as well as LES and DNS. Throughout this work, it has been observed that increasing the spatial order of accuracy consistently improves the quality of the results obtained, suggesting that the use of such high order schemes can be beneficial. The increase in computational effort, however, is not negligible when using higher order schemes, and an investigation of the error to cost ratio has been performed. This suggests that the order of the most efficient scheme will depend on the level of error that is acceptable for a given simulation. However, for the test problems considered, namely the inviscid convection of a vortex and the LES of a turbulent pipe flow, fourth order accuracy was found more efficient that second order accuracy. Sixth order accuracy was found to be excessively expensive. One should analyze for a simulation the different sources of errors from time integration, spatial discretization, and physical models, and adapt the accuracy of the numerical scheme in order to ensure that the spatial discretization errors are not dominant.

Acknowledgments

The authors wish to express their gratitude to Mr. Ed Knudsen for his immense help in the development of the code used for the simulations in this paper. We are also thankful to Mr. Shashank and Dr. Vincent Moureau for their fruitful comments on a draft of this manuscript. We also gratefully acknowledge funding by NASA and by the DOE through the ASC program.

References

[1] J.H. Ferziger, M. Peric, Computational Methods for Fluid Dynamics, third ed., Springer, Berlin, 2002.
[2] A.G. Kravchenko, P. Moin, On the effect of numerical errors in large eddy simulations of turbulent flows, J. Comput. Phys. 131 (1997) 310–322.
[3] S.A. Orszag, On the elimination of aliasing in finite-difference schemes by filtering high-wavenumber components, J. Atmos. Sci. 28 (1971) 1074.
[4] G.S. Patterson, S.A. Orszag, Spectral calculations of isotropic turbulence: efficient removal of aliasing interactions, Phys. Fluids 14 (1971) 2538–2541.
[5] S.K. Lele, Compact finite-difference schemes with spectral-like resolution, J. Comput. Phys. 103 (1992) 16–42.
[6] R. Mittal, P. Moin, Suitability of upwind-biased finite difference schemes for large-eddy simulation of turbulent flows, AIAA J. 35 (1997) 1415–1417.
[7] M. Park, J.Y. Yoo, H. Choi, Discretization errors in large eddy simulation: on the suitability of centered and upwind-biased compact difference schemes, J. Comput. Phys. 198 (2004) 580–616.

[8] F.H. Harlow, J.E. Welch, Numerical calculation of time-dependent viscous incompressible flow of fluid with free surface, Phys. Fluids 8 (1965) 2182–2189.
[9] K. Akselvoll, P. Moin, Large-eddy simulation of turbulent confined coannular jets, J. Fluid Mech. 315 (1996) 387–411.
[10] C.D. Pierce, P. Moin, Progress-variable approach for large eddy simulation of turbulent combustion, Rep. TF80, Flow Physics and Computation Division, Dept. Mech. Eng., Stanford Univ., 2001.
[11] T.C. Treurniet, F.T.M. Nieuwstadt, B.J. Boersma, Direct numerical simulation of homogeneous turbulence in combination with premixed combustion at low mach number modelled by the *G*-equation, J. Fluid Mech. 565 (2006) 25–62.
[12] R. Verzicco, P. Orlandi, A finite-difference scheme for three-dimensional incompressible flows in cylindrical coordinates, J. Comput. Phys. 123 (1996) 402–414.
[13] T.S. Lund, P. Moin, Large-eddy simulation of a concave wall boundary layer, Int. J. Heat Fluid Flow 17 (1996) 290–295.
[14] S. Nagarajan, S.K. Lele, J.H. Ferziger, A robust high-order compact method for large eddy simulation, J. Comput. Phys. 191 (2003) 392–419.
[15] Y. Morinishi, T.S. Lund, O.V. Vasilyev, P. Moin, Fully conservative higher order finite difference schemes for incompressible flow, J. Comput. Phys. 143 (1998) 90–124.
[16] F. Nicoud, Conservative high-order finite difference schemes for low-mach number flows, J. Comput. Phys. 158 (2000) 71–97.
[17] O.V. Vasilyev, High order finite difference schemes on non-uniform meshes with good conservation properties, J. Comput. Phys. 157 (2000) 746–761.
[18] Y. Morinishi, O.V. Vasilyev, T. Ogi, Fully conservative finite difference scheme in cylindrical coordinates for incompressible flow simulations, J. Comput. Phys. 197 (2004) 686–710.
[19] R.W. Bilger, Turbulent flows with nonpremixed reactants, in: P.A. Libby, F.A. Williams (Eds.), Turbulent Reacting Flows, Springer-Verlag, Berlin, 1980.
[20] X.-D. Liu, S. Osher, T. Chan, Weighted essentially non-oscillatory schemes, J. Comput. Phys. 115 (1994) 200–212.
[21] G.S. Jiang, C.W. Shu, Efficient implementation of weighted ENO schemes, J. Comput. Phys. 126 (1996) 202–228.
[22] R.R. Nourgaliev, T.G. Theofanous, High-fidelity interface tracking in compressible flows: unlimited anchored adaptive level set, J. Comput. Phys. 224 (2007) 836–866.
[23] B.P. Leonard, A stable and accurate convective modelling procedure based on quadratic upstream interpolation, Comput. Methods Appl. Mech. Eng. 19 (1979) 59–98.
[24] J. Kim, P. Moin, Application of a fractional-step method to incompressible Navier–Stokes equations, J. Comput. Phys. 59 (1985) 308–323.
[25] H.A. van der Vorst, Iterative Krylov Methods for Large Linear Systems, first ed., Cambridge University Press, Cambridge, 2003.
[26] R.D. Falgout, U.M. Yang, Hypre: a library of high performance preconditioners, in: P.M.A. Sloot, C.J.K. Tan, J.J. Dongarra, A.G. Hoekstra (Eds.), Computational Science – ICCS 2002 Part III, vol. 2331, Springer-Verlag, Berlin, 2002.
[27] H. Choi, P. Moin, Effects of the computational time step on numerical solutions of turbulent flow, J. Comput. Phys. 113 (1994) 1–4.
[28] F.E. Ham, F.S. Lien, A.B. Strong, A fully conservative second-order finite different scheme for incompressible flow on nonuniform grids, J. Comput. Phys. 177 (2002) 117–133.
[29] T.S. Lundgren, Linearly forced isotropic turbulence, in: Annual Research Briefs, Center for Turbulence Research, Stanford, 2003.
[30] V. Eswaran, S.B. Pope, Direct numerical simulations of the turbulent mixing of a passive scalar, Phys. Fluids 31 (1988) 506–520.
[31] I. Orlanski, A simple boundary condition for unbounded hyperbolic flows, J. Comput. Phys. 21 (1976) 251–269.
[32] R.L. Sani, J. Shen, O. Pironneau, P.M. Gresho, Pressure boundary condition for the time-dependent incompressible Navier–Stokes equations, Int. J. Numer. Methods Fluids 50 (2006) 673–682.
[33] P.M. Gresho, Incompressible fluid dynamics: some fundamental formulation issues, Annu. Rev. Fluid Mech. 23 (1991) 413–453.
[34] J.G.M. Eggels, F. Unger, M.H. Weiss, J. Westerweel, R.J. Adrian, R. Friedrich, F.T.M. Nieuwstadt, Fully developed turbulent pipe flow: a comparison between direct numerical simulation and experiment, J. Fluid Mech. 268 (1994) 175–209.
[35] K. Fukagata, N. Kasagi, Highly energy-conservative finite difference method for the cylindrical coordinate system, J. Comput. Phys. 181 (2002) 478–498.
[36] G.S. Constantinescu, S.K. Lele, A highly accurate technique for the treatment of flow equations at the polar axis in cylindrical coordinates using series expansions, J. Comput. Phys. 183 (2002) 165–186.
[37] V.V. Meleshko, G.J.F. Heijst, On chaplygin's investigations of two-dimensional vortex structures in an inviscid fluid, J. Fluid Mech. 272 (1994) 157–182.
[38] P.K. Yeung, S.B. Pope, Lagrangian statistics from direct numerical simulations of isotropic turbulence, J. Fluid Mech. 207 (1989) 531–586.
[39] C. Rosales, C. Meneveau, Linear forcing in numerical simulations of isotropic turbulence: physical space implementations and convergence properties, Phys. Fluids 17 (2005) 095106-1–095106-8.
[40] G. Comte-Bellot, S. Corrsin, Simple Eulerian time correlation in full and narrow band velocity signals in grid generated, isotropic turbulence, J. Fluid Mech. 48 (1971) 273–337.
[41] M. Germano, U. Piomelli, P. Moin, W.H. Cabot, A dynamic subgrid-scale eddy viscosity model, Phys. Fluids A 3 (1991) 1760–1765.
[42] D.K. Lilly, A proposed modification of the Germano subgrid-scale closure method, Phys. Fluids A 4 (1992) 633–635.
[43] S. Ghosal, An analysis of numerical errors in large-eddy simulations of turbulence, J. Comput. Phys. 125 (1996) 187–206.

[44] F.K. Chow, P. Moin, A further study of numerical errors in large-eddy simulations, J. Comput. Phys. 184 (2003) 366–380.
[45] C. Meneveau, T.S. Lund, W.H. Cabot, A Lagrangian dynamic subgrid-scale model of turbulence, J. Fluid Mech. 319 (2000) 353–385.
[46] M. Amielh, T. Djeridane, F. Anselmet, L. Fulachier, Velocity near-field of variable density turbulent jets, Int. J. Heat Mass Transfer 39 (1996) 2149–4164.
[47] T. Djeridane, M. Amielh, F. Anselmet, L. Fulachier, Velocity turbulence properties in the near-field region of axisymmetric variable density jets, Phys. Fluids 6 (1996) 1614–1630.
[48] J. Réveillon, L. Vervisch, Response of the dynamic LES model to heat release induced effects, Phys. Fluids 8 (1996) 2248–2250.